
Master Thesis

Coarse-Graining of Responsive Colloids

AUTHOR: JAN-PHILIPP MAURER
SUPERVISED BY: PROF. DR. JOACHIM DZUBIELLA
Physikalisches Institut
Universität Freiburg
Hermann-Herder-Str. 3, 79104 Freiburg, Germany

November 18, 2025



Abstract

Responsive colloids consist of micro-sized, soft particles whose properties, such as size, shape, or charge, can change in response to external stimuli such as pH values or temperature. Understanding their behavior requires simulations that can capture this responsiveness in a computationally efficient manner. In this thesis, we employ a coarse-grained model with an additional degree of freedom to reproduce the simulation data from a specific detailed beads-network simulations of responsive colloids. Our primary objective is to identify suitable one- and two-body interaction potentials. To achieve this, we fit various functions to the low-density emergent size distribution from the beads-network simulation to define the one-body term. For the two-body interaction, we utilize a Hertzian potential, the strength of which will be determined by calculating an effective potential from both interaction terms and comparing it to that of the beads-network simulation. The simulations update particle positions and size degrees of freedom using Brownian dynamics. Although the coarse-grained models simulation data differ quantitatively from the reference simulations, they successfully replicated key structural and dynamical trends, indicating progress in finding suitable one- and two-body interactions that reproduce the beads-network simulation data.

Acknowledgments

I would like to sincerely thank Giovanni Del Monte and Emanuela Zaccarelli for generously providing their simulation data used in this work. The data was instrumental not only for validating and comparing results but also served as the foundation for deriving the interaction and property potentials applied in this study. Their support greatly contributed to the progress and quality of this research.

I would also like to thank the state of Baden-Württemberg for its support of bwHPC and the German Research Foundation (DFG) for funding under "Project number 455622343" (bwForCluster NEMO 2).

Language editing and grammar corrections were assisted by the AI-based tools Writefull (Writefull B.V., 2025) and ChatGPT (OpenAI, 2025). The content, analysis, and interpretations presented in this thesis are entirely the author's own, if not cited otherwise.

Contents

1	Introduction	1
2	Theoretical Background	4
2.1	Brownian Dynamics	4
2.2	The Hertzian Model	5
2.3	The Fuzzy Sphere Model	5
2.4	Statistical and other Quantities	6
3	Beads-Network Model	10
4	Models and Methods	12
4.1	Coarse-Grained Responsive Colloids	12
4.2	Computational Model and Simulation Details	13
5	Results and Discussion	15
5.1	Property Potential	15
5.2	Interaction Potential	17
5.3	Emergent Size Distribution	20
5.4	Bulk Modulus	26
5.5	Radial-Distribution Function	29
5.6	Mean Squared Displacement	31
5.7	Different Property potentials	33
5.7.1	Polynomial Order Two	33
5.7.2	FENE Potential	39
6	Conclusion and Outlook	47
7	Appendix	49
7.1	Transformation from Radius of Gyration to Real Diameter	49
7.2	Plots and Tables for second order polynomial	50
7.3	Plots and Tables for the FENE potentials	53

List of Figures

1	Sketch and density profile of a fuzzy sphere colloid.	6
2	Snapshot of the beads-network simulations.	11
3	Fit Ψ data with polynomial of order 4.	17
4	Finding an interaction potential.	20
5	RC snapshot of different packing fractions.	21
6	Reproduction: Snapshot of the beads-network simulations.	22
7	Emergent size distributions for different packing fractions.	23
8	Mean and Variance of the particle sizes for the CG model with the property potential $\Psi_4^{\text{poly}}(\sigma)$.	24
9	Effective packing fraction of our CG model with the property potential $\Psi_4^{\text{poly}}(\sigma)$.	25
10	Bulk modulus of individual particles of our CG model with the property potential $\Psi_4^{\text{poly}}(\sigma)$.	27
11	Pressure and bulk modulus of the system of our CG model with the property potential $\Psi_4^{\text{poly}}(\sigma)$.	28
12	Radial distribution Function of the CG model with property potential $\Psi_4^{\text{poly}}(\sigma)$.	29
13	Main RDF peak position and height comparison CG, BN and non-responsive CG.	31
14	Mean squared displacement of the CG model with property potential $\Psi_4^{\text{poly}}(\sigma)$.	32
15	Mean squared displacement of the BN model.	33
16	Fit Ψ data with polynomial of order 2.	34
17	Mean and Variance of the particle sizes of the CG model with the property potential $\Psi_2^{\text{poly}}(\sigma)$.	35
18	Bulk modulus of individual particles and the whole system for CG simulations with a second-order polynomial as the property potential.	37
19	Radial distribution Function of $\Psi_2^{\text{poly}}(\sigma)$.	38
20	Fit Ψ data with a FENE potential.	40
21	Mean and Variance of the particle sizes for CG model based on FENE as Ψ .	41
22	Bulk modulus of individual particles for CG models based on FENE as Ψ .	42
23	Bulk modulus of the whole system for CG models based on FENE as Ψ .	43
24	Radial distribution function of FENE with $R = 15.5$	44
25	Radial distribution function of FENE with $R = 16$	45
26	Mean squared displacement of different packing fractions for CG models based on FENE as Ψ .	46
27	Emergent size distributions for different packing fractions of model with $\Psi(\sigma) = \Psi_2^{\text{poly}}(\sigma)$.	50

28	Effective packing fraction of the model with $\Psi(\sigma) = \Psi_2^{\text{poly}}(\sigma)$	51
29	System pressure of the model with $\Psi(\sigma) = \Psi_2^{\text{poly}}(\sigma)$	51
30	Mean squared displacement of the model with $\Psi(\sigma) = \Psi_2^{\text{poly}}(\sigma)$	52
31	Fit Ψ data with a FENE potential.	53
32	Emergent size distributions of the models with $\Psi(\sigma) = \Psi_R^{\text{FENE}}(\sigma)$	54
33	Effective packing fraction of the models with $\Psi(\sigma) = \Psi_R^{\text{FENE}}(\sigma)$	55
34	System pressure of the models with $\Psi(\sigma) = \Psi_R^{\text{FENE}}(\sigma)$	56
35	Comparison of the effective potential of the BN model and the CG models.	57
36	Comparison of the emergent size distributions of the BN model and the CG model with $\Psi_{R=16}^{\text{FENE}}$	58

List of tables

1	Behavior of different quantities in the BN model.	11
2	Fit parameters of polynomial order 4.	16
3	Fit parameters of polynomial order 2.	50
4	Fit parameters of FENE potentials.	53

1 Introduction

Colloids are mixtures of two substances, in which one of them is uniformly distributed within the other. They range in size from one nanometer to one micrometer, making them significantly larger than particles in a solvent but still small enough to undergo Brownian motion. Because of their scale, the physical behavior of colloidal systems differs from that of both molecular/atomic and macroscopic systems. Colloidal systems can be found in a wide range of biological, industrial, and consumer products, including macromolecules, soft materials, cosmetics, and food. This broad relevance makes colloids an interesting topic of research [1–5]. Especially responsive colloids (RC) are the subject of a lot of current works in both experimental [6–12] and theoretical research [13–19]. RCs are colloids that change their properties in response to a variety of stimuli, for example temperature [20], magnetic or electric fields [21], and the chemical environment [22, 23]. Their response can include changes such as size, shape, surface charge, or interparticle interactions based on the stimulus. This adjustability makes RCs promising components in complex applications, such as drug delivery systems [22, 24], smart materials[25] and for sensing applications [26].

A specific type of responsive colloids that have gained attention in recent years are microgels [1, 3, 26, 27]. Microgels are soft, (typically) water-dispersed particles made of cross-linked 3D polymer networks [1], usually larger than 100 nm [26]. Their properties, such as size, shape, and swelling behavior, are tunable via synthesis conditions [26, 27]. A common example is poly(N-isopropylacrylamide) (PNIPAM) microgels [1, 3], which undergo a volume phase transition (VPT) near $T_{\text{VPT}} \approx 32^\circ\text{C}$, changing from a swollen state to a collapsed state [1, 27].

In general, simulations are an essential tool for studying physical systems when experiments are limited or when analyzing fundamental behavior. Consequently, colloidal systems can be approached from various computational perspectives.

One such approach is the all-atom simulation, in which individual atoms are represented as the smallest units that assemble into larger molecules. Such simulations are particularly useful for describing the behavior of individual colloidal particles, including their inner structure, such as hydrogen bonds, or charge effects. However, all-atoms simulations rely on accurate interatomic potentials and are typically restricted to systems of one or only a few of such macromolecules, due to high computational costs.

Another common approach are beads-network (BN) simulations, in which colloidal particles are represented by beads chained together through spring-like potentials [16, 19, 28]. Here, the beads serve as the smallest units, each representing a cluster of atoms or smaller molecules such as monomers. This coarse-grained(CG) perspective gives the possibility to simulate much larger systems over longer time periods, by reducing the degrees of freedom. Despite this simplification, the inner structure and dynamics of the particles can still be captured, while quantities such as elasticity, interaction strength

and responsiveness can be directly controlled. This makes the approach useful for comparisons with theoretical predictions or experimental data. However, this method has its limits. Chemical details or reactions are lost (if not implemented directly), and solvent effects that are often only represented indirectly, for example, through friction terms. Furthermore, the simulated macromolecules still consist of several hundreds to a few thousand beads, making them costly to compute.

A simpler and computationally more efficient approach is provided by particle-based coarse-grained simulations, in which each colloid is represented as a single spherical particle with fixed parameters. In this representation, the system is fully described by the particles' positions and their effective interaction potentials. This level of coarse-graining dramatically reduces the number of degrees of freedom compared to bead-spring or network-based models. However, it also introduces challenges, such as the accurate parameterization of effective interactions and the complete loss of information about the internal structure and dynamics of individual particles.

An improvement of such simple CG models is the CG responsive colloid model, in which each colloidal particle is represented by a simple sphere with an extra degree of freedom [13, 15, 18]. This framework, originally developed by Lin *et al.* [13], introduces an additional collective variable that represents an internal property of the particle (e.g., particle diameter), thereby giving each particle an extra degree of freedom at the coarse-grained level. From this formulation, a CG free-energy function is derived, consisting of a one-body term that encodes the property distribution of an isolated particle, and many body contributions. Similar to the simple non-responsive CG level from above, this approach significantly reduces the number of degrees of freedom compared to beads-network simulations, making it both simple and computationally efficient. In addition, it retains the ability to capture responsiveness to external stimuli. However, challenges for this model are the accurate parameterization of interaction potentials or inner property potentials from experiments or more detailed simulations. Moreover, because of the simplified structure, effects related to particle deformation and internal dynamics are lost.

An example of the application of the CG responsive colloid model is presented by Baul and Dzubiella in [15], where the CG framework was used to perform Brownian dynamics simulations of suspensions of soft hydrogel colloids, with the diameter of the particles serving as the inner property. In this master's thesis, we perform similar simulations using the same methodological framework.

For this thesis, our aim is to develop a CG model within this framework that is capable of describing the more complex system of realistic microgel particles in the swollen state, performed by Del Monte and Zaccarelli and presented in the paper "Numerical study of neutral and charged microgel suspensions: from single-particle to collective behavior" [16]. In their work, they performed molecular dynamics simulations of microgels over a wide range of particle densities, represented as bead networks composed of monomers of constant size.

Therefore, our main goal is to determine potential functions suitable for describing the one-body term of the BN microgels, as well as the many-body interactions. For parameterization, we use simulation data from their low-density limit. To evaluate the performance of our CG model, we compare key quantities—such as individual particle size distributions and radial distribution functions—with the corresponding results from the BN model of Del Monte and Zaccarelli.

The thesis begins with an overview of the key physical concepts required for coarse-grained (CG) simulations. This includes a brief introduction to Brownian dynamics as well as relevant statistical quantities and concepts. The following chapter discusses the computational model and simulation details. Subsequently, the BN simulations of Del Monte and Zaccarelli are presented, along with the specific results used in this work. Based on these data, we then determine the property potential $\Psi(\sigma)$ and the interaction potential $\phi(r, \sigma_i, \sigma_j)$ using the low-density limit. The results of our CG simulations are presented next and compared to those of the BN system. Finally, we conclude with a discussion of the findings and an outlook on possible directions for future research.

2 Theoretical Background

2.1 Brownian Dynamics

Brownian dynamics is a simulation method commonly used to model the movements of small particles in a fluid. On the length scale of macromolecular particles, such as colloids, stochastic collisions from the fluid molecules become the leading force. This results in a random walk of the particles in the liquid, known as Brownian motion. The diffusion coefficient D characterizes the speed with which the particles spread throughout the system over time under Brownian motion. This is illustrated by the "diffusion law" given as [29]

$$\langle \mathbf{x}^2(t) \rangle = 2dDt \quad (1)$$

where $\langle \mathbf{x}^2(t) \rangle$ is the mean-squared displacement of the position vector \mathbf{x} and the number of spatial dimensions d .

This Brownian behavior is modeled by extending the Newton equation of motion with a friction term and a random force [29]. The resulting equation of motion is often called the Langevin equation. In the following, the formulation of the Langevin equation is taken from Schuss [30], but friction γ is not scaled per unit mass.

$$m\ddot{x} + \gamma\dot{x} + U'(x) = \sqrt{2\gamma k_B T} \dot{w} \quad (2)$$

Here x is the position of the particles, with \dot{x} and \ddot{x} representing the first and second time derivatives, respectively. γ is the friction coefficient, $U'(x)$ is the position derivative of the potential energy $U(x)$ representing the force, $k_B T$ is the thermal energy of the system and m is the mass of the particles. The last term represents thermal fluctuations modeled as Gaussian white noise $\dot{w}(t)$, which is the time derivative of a Wiener process $w(t)$. The Wiener process is a stochastic process with zero mean and variance proportional to time, providing a mathematical description of Brownian motion [30]. In the case of Brownian dynamics, the friction forces dominate the whole motion process, while inner effects are negligible.

With $\gamma \rightarrow \infty$ in eq. (2), we arrive to the so-called Smoluchowski limit [30] as

$$\dot{x} = -\frac{U'(x)}{\gamma} + \sqrt{\frac{2k_B T}{\gamma}} \dot{w}. \quad (3)$$

This extreme case represents the overdamped/high friction limit present in Brownian motion. If we now use the Einstein relation [30]

$$D = \frac{k_B T}{\gamma} \quad (4)$$

we can rewrite eq. (3) as

$$\dot{x} = -\frac{D}{k_B T} U'(x) + \sqrt{2D} \dot{w}. \quad (5)$$

This first-order stochastic differential equation can be discretized using Euler integration as

$$x(t + \Delta t) = x(t) - \frac{D}{k_B T} U'(x) \Delta t + \sqrt{2D\Delta t} R_n \quad (6)$$

with R_n being a random number from a normal distribution with mean zero and variance one.

2.2 The Hertzian Model

The Hertzian model refers to a type of interaction potential that describes the effective repulsion between two elastic spheres within the framework of classical elasticity theory [28]. The potential is thereby given by [15]

$$\phi(r, \sigma_i, \sigma_j) = \epsilon \left(1 - \frac{r}{\sigma_{ij}}\right)^{5/2} \Theta\left(1 - \frac{r}{\sigma_{ij}}\right). \quad (7)$$

Here, ϵ dictates the strength of the interaction, and $\sigma_{ij} = \frac{\sigma_i + \sigma_j}{2}$. Θ denotes the Heaviside function, restricting the potential to distances $r < \sigma_{ij}$ and otherwise returning zero. Due to our extra degree of freedom, the diameter of the particle σ , we need to account for the size dependence of $\epsilon = \epsilon(\sigma_i, \sigma_j)$. This arises from a direct connection between the elastic properties of the soft colloid particles and the strength of the interaction [18, 28]. For notational convenience, we define the support function $A(\sigma_i)$ [18]

$$A(\sigma_i) = \frac{Y(\sigma_i)}{1 - \nu(\sigma_i)^2}, \quad (8)$$

where $Y(\sigma_i)$ is the Young modulus and $\nu(\sigma_i)$ is the Poisson ratio of the soft particle. A mathematical expression for $\epsilon(\sigma_i, \sigma_j)$ is given by [18]

$$\epsilon(\sigma_i, \sigma_j) = \frac{8}{15} A_{\text{eff}}(\sigma_i, \sigma_j) \left(\frac{\sigma_i + \sigma_j}{2}\right)^2 \left(\frac{\sigma_i \sigma_j}{4}\right)^{1/2}, \quad (9)$$

where

$$A_{\text{eff}}(\sigma_i, \sigma_j) = \frac{A(\sigma_i)A(\sigma_j)}{A(\sigma_i) + A(\sigma_j)}. \quad (10)$$

2.3 The Fuzzy Sphere Model

Soft microgels, such as poly(N-isopropylacrylamide) (PNIPAM), with low crosslinking density, have been found to have a fuzzy outer structure and do not follow a constant density profile [9]. Such RCs can be described by the fuzzy sphere model, characterized by an inhomogeneous density profile that gradually decays from the outer shell, resembling a fuzzy, hairy sphere[31]. The model describes the structure of the particle as a hard core of radius R_C with constant density, while the outer shell is described by half its width σ_{surf} with a density that decays to zero [9, 32]. Figure 1 (a) shows a sketch

of the structure of a fuzzy-sphere colloid with its inner core and outer fuzzy corona. This gives us the total radius of the fuzzy sphere colloid as

$$R = R_C + 2\sigma_{\text{surf}}. \quad (11)$$

The density profile of fuzzy spheres is typically described by combining a solid sphere profile with a Gaussian function [31]. A common way to describe this density profile mathematically is using a complementary error function [31, 33]

$$\rho_{\text{Sphere}}^{\text{Fuzzy}}(r) = \begin{cases} \rho_0, & \text{for } r \leq R_C \\ \rho_0 \cdot \text{erfc}\left(\frac{r - R_C}{\sqrt{2}\sigma_{\text{surf}}}\right), & \text{for } r > R_C \end{cases} \quad (12)$$

Here ρ_0 is the constant density of the core. This gives us a density profile that is constant until $r > R_C$ and then decreases to zero after the shell ends. An example plot of this behavior is shown in fig. 1 (b) with arbitrarily chosen parameters $\rho_0 = 1.0$, $R_C = 0.7$, and $\sigma_{\text{surf}} = 0.15$ for illustration.

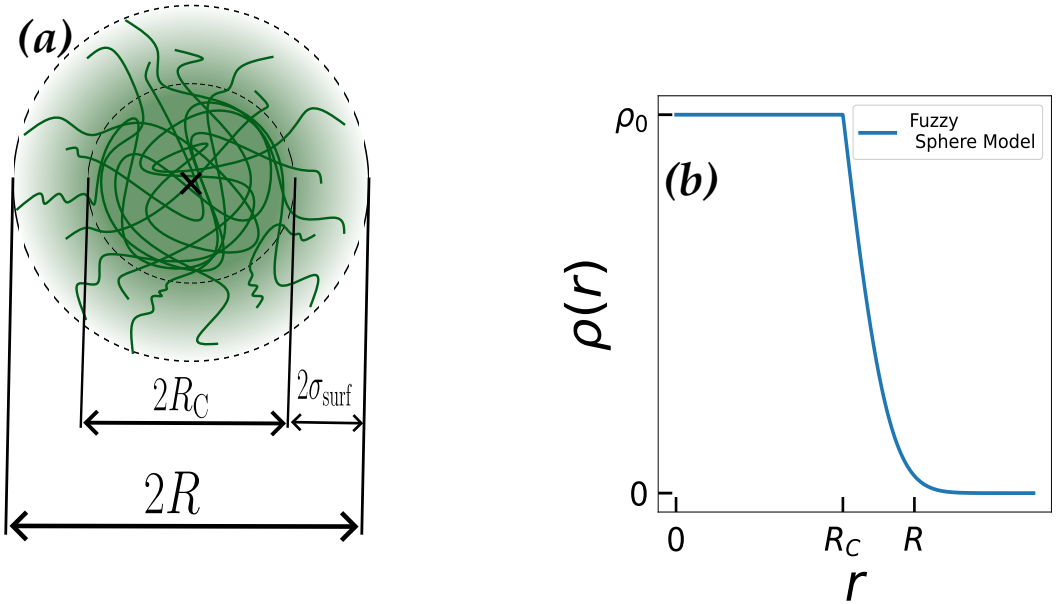


Figure 1: (a): Sketch of a fuzzy sphere particle showing the inner structure with the inner core having the radius R_C and the outer fuzzy shell with width $2\sigma_{\text{surf}}$. This gives the particle a total radius of $R = R_C + 2\sigma_{\text{surf}}$. (b): Density profile of a fuzzy sphere particle following eq. (12) with arbitrarily chosen parameters.

2.4 Statistical and other Quantities

System Pressure

In the canonical ensemble (NVT), the pressure P is not a controlled variable of the system. It can be calculated from microscopic quantities using statistical mechanics, for

example, via the virial equation [34]

$$PV = Nk_B T - \frac{1}{3} \left\langle \sum_{i=1}^N \mathbf{r}_i(t) \cdot \mathbf{F}_i(t) \right\rangle. \quad (13)$$

Here, $\mathbf{r}_i(t)$ is the position vector and $\mathbf{F}_i(t)$ is the total interaction force of particle i . In a system with no particle interactions, this relation reduces to the ideal gas equation.

Bulk Modulus K

The bulk modulus K of a material is a measure of its resistance of the material to bulk compression. It is defined as the ratio of the infinitesimal increase in pressure to the resulting relative decrease in volume [35]:

$$K = -V \frac{dP}{dV}, \quad (14)$$

where V is the initial volume of the system and P is the pressure of the system. An incompressible material has a bulk modulus of $K \rightarrow \infty$.

For individual microgels, we can also calculate a bulk modulus K_p using spontaneous volume fluctuations through [16]

$$K_p = k_B T \frac{\langle V_i \rangle}{\langle V_i^2 \rangle - \langle V_i \rangle^2}. \quad (15)$$

Poisson Ratio ν

The Poisson ratio ν is a measure of the deformation of a material in the direction perpendicular to the loading direction. Thus, following Hooke's law, the transverse strain $\Delta d/d$ is proportional to the axial strain $\Delta l/l$, defining the Poisson ratio [35]

$$\nu = \frac{\Delta d/d}{\Delta l/l}. \quad (16)$$

For an incompressible material, with $K \rightarrow \infty$, the Poisson ratio is exactly $\nu = 0.5$.

Young Modulus Y

The Young modulus is defined as the ratio of stress applied to an object and the resulting axial deformation in the linear elastic region. It can be calculated by [35]

$$Y = \frac{F/A}{\Delta L/L_0}. \quad (17)$$

Here, F/A is the applied force per area, L_0 is the original length and ΔL is the change in length. For cross-linked polymer microgels, the Young modulus scales with the particle volume [18]:

$$Y(\sigma) \propto \frac{1}{\sigma^3}. \quad (18)$$

Radial Distribution function

The radial distribution function (RDF), typically denoted $g(r)$, is a fundamental quantity in statistical mechanics and molecular simulations. $g(r)$ can be interpreted as the conditional probability of finding a second particle at a distance r with the position of the first one as the origin and is defined as [34]

$$g(r) = \frac{1}{\rho N} \left\langle \sum_{i=1}^N \sum_{j=1}^N \delta(r - r_{ij}) \right\rangle, \quad (19)$$

where N is the particle number and ρ is the number density. In simulations, $g(r)$ is calculated by creating a histogram around particles in shells of size Δr at distance r [29]

$$g(r) = \frac{\langle n \rangle}{\Delta V(r)\rho}. \quad (20)$$

Here, $\Delta V = 4\pi r^2 \Delta r$ and $\langle n \rangle$ is the number of particles in the shell averaged over time.

Radius of gyration

The radius of gyration R_g is defined as the average squared distance between the monomers and the center of mass of a polymer [36]:

$$R_g^2 = \frac{1}{n} \sum_{i=1}^n \langle (\mathbf{r}_i - \mathbf{r}_{\text{com}})^2 \rangle. \quad (21)$$

Here, n is the number of monomers, \mathbf{r}_i is the position of the monomer i and \mathbf{r}_{com} is the position of the center of mass. For a continuous density profile $\rho(r)$, we can calculate R_g via

$$R_g^2 = \frac{\int r^2 \rho(r) d\mathbf{r}}{\int \rho(r) d\mathbf{r}}. \quad (22)$$

The lower integral is for normalization.

Mean Squared Displacement

The mean squared displacement (MSD) measures the displacement of a particle over time. It is defined as

$$\langle [\mathbf{r}(t) - \mathbf{r}(0)]^2 \rangle, \quad (23)$$

where $\mathbf{r}(0)$ and $\mathbf{r}(t)$ are the positions of the particles at time 0 and t , respectively. The MSD thus describes how far, on average, a particle moves from its initial position. It is also related to the self-diffusion coefficient D_{eff} through the Einstein relation [34]:

$$D_{\text{eff}} = \lim_{t \rightarrow \infty} \frac{\langle [\mathbf{r}(t) - \mathbf{r}(0)]^2 \rangle}{6t}. \quad (24)$$

This relation provides a direct connection between the slope of the MSD curve at long times and the diffusive dynamics of the system.

The FENE potential

The finitely extensible nonlinear elastic potential, or FENE potential, is a bound potential commonly used to describe bead-spring chains in CG polymer simulations. In comparison to a simple harmonic spring potential, it includes a maximum extension beyond the bond can not stretch. A typical form for the FENE potential is [19]

$$U_{\text{FENE}}(r) = -\frac{1}{2}kR_0^2 \log(1 - (r/R_0)^2), \quad (25)$$

where k is the spring constant, R_0 is the maximum extension of the bond and r is the length of the bond.

3 Beads-Network Model

The following section will present the beads network (BN) simulation described in the paper "Numerical study of neutral and charged microgel suspensions: from single-particle to collective behavior" by Del Monte and Zaccarelli [16]. We will provide a brief introduction to the BN model used to simulate single responsive particles and discuss the simulation, as well as the resulting data used in the following section of the thesis. While Del Monte and Zaccarelli also present results of charged microgels, we will only use and discuss the results of their neutral particles.

Beads-Network Model

Del Monte and Zaccarelli performed molecular dynamics simulations of an ensemble of microgel particles under swollen conditions. The individual microgels are therefore made up of a connected network of $N_M \sim 5000$ monomers represented by beads. They are individually simulated with a coarse-grained model described by Ninarello *et al.* [27] with a cross-linker molar fraction of $c = \simeq 5.0\%$. In assembled microgels, the monomers are bonded to chains via a Finitely Extensible Non-linear Elastic (FENE) potential and can interact with each other through a Weeks-Chandler-Andersen (WCA) potential [16]. The unit length scale here is the constant monomer diameter σ_M , which will also be used as the unit length scale of our CG RC simulation.

Beads Network Simulation and Simulation data

For the main simulation run 27, individual microgels were created as previously stated and then replicated four times to get a total number of $N_{BN} = 108$ microgels. The BN system was then equilibrated for 10^7 time steps, followed by a production run of 10^8 time steps. Figure 2 shows Snapshots of simulations at different packing fractions η . Here, we can clearly see the beads-network structure of the individual microgels and their behavior at high densities. The latter will be discussed in more detail in the next chapter, when we compare our results with those of Del Monte and Zaccarelli.

Del Monte and Zaccarelli provided us with the results of their simulations for different packing fractions η . Specially, their emergent size distribution $\tilde{p}_\eta^{BN}(R_g)$ and radial distribution functions $g(r)$. The emergent size distribution $\tilde{p}_\eta^{BN}(R_g)$ denotes a statistical distribution of all particle sizes over all time steps. From these two quantities, we aim to extract a one- and two-body interaction for our CG simulation. Other quantities are taken directly from their paper [16].

Afterwards, we will compare these and other quantities of the BN model with those obtained from our CG model, specifically: the mean particle diameter $\langle \sigma \rangle$ and its variance $\langle \sigma^2 \rangle - \langle \sigma \rangle^2$, the individual particle and system bulk moduli K_p and K , the radial distribution function $g(r)$, and the mean squared displacement $\langle [\mathbf{r}(t) - \mathbf{r}(0)]^2 \rangle$.

Our goal is to reproduce the behavior observed in the BN model for our CG model, as summarized in table 1.

Table 1: Behavior of different quantities in the BN model.

Quantity	Trend in BN model
$\langle \sigma \rangle$	particle shrinkage starting around $\eta = 0.8$, reaching $\approx 29 \sigma_M$ at highest density
$\langle \sigma^2 \rangle - \langle \sigma \rangle^2$	variance decrease starting around $\eta = 0.8$, reaching $\approx 0.5 \sigma_M^2$ at highest density
K_p	increase with η , in same order of magnitude
K	increase with η , in same order of magnitude
$g(r)$	re-entering of main peak height at high packing fractions
$\langle [\mathbf{r}(t) - \mathbf{r}(0)]^2 \rangle$	slowdown in dynamics towards a glass-like state

The emergent size distribution $\tilde{p}_\eta^{\text{BN}}(R_g)$ is given as a function of the radius of gyration R_g . Since our simulation deals with the real diameter σ of the RC particles, we need a transformation $R_g \rightarrow \sigma$ to enable comparison. The derivation for this transformation can be found in the Appendix section 7.1 and results in

$$\sigma(R_g) = 2 \cdot \left(\frac{5}{3} \sqrt{\frac{\pi}{2}} \frac{R_g^2}{R_C} - \left(\sqrt{\frac{\pi}{2}} - 1 \right) R_C \right). \quad (26)$$

We take the core radius R_C from the results of Del Monte and Zaccarelli based on Figure 4(b) in [16].

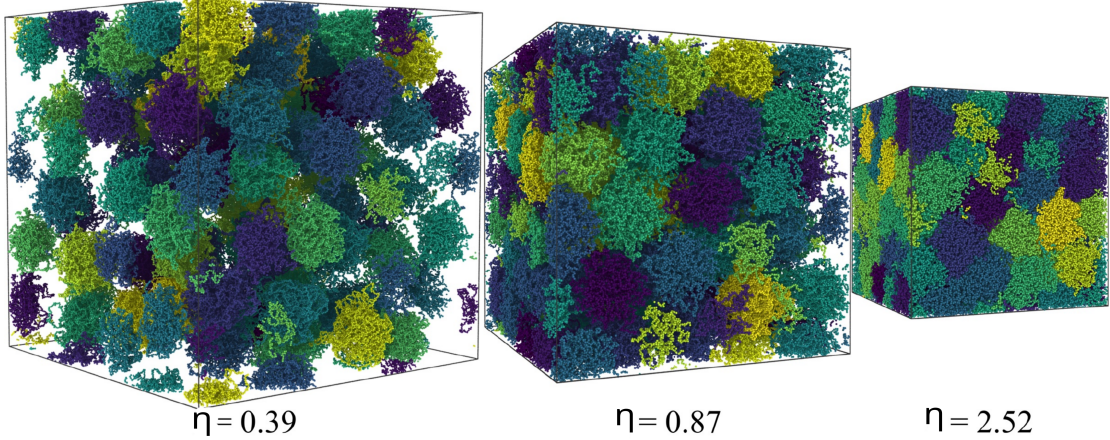


Figure 2: Snapshot of a microgel suspensions from the BN model at a packing fractions $\eta = 0.39, 0.87$ and 2.52 , from left to right. Figure taken from Ref. [16]. Published under the terms of the Creative Commons Attribution 4.0 International License (CC BY 4.0).

4 Models and Methods

4.1 Coarse-Grained Responsive Colloids

The next step is to define a model to describe CG soft responsive colloids with an additional property degree of freedom. The statistical mechanical approach used in the following to describe coarse-grained responsive colloids closely follows the model used by Baul and Dzubiella [15], while the underlying framework was first proposed by Lin *et al.* [13]:

Our system consists of a liquid of N_{RC} responsive colloid particles interacting in a three-dimensional cube of volume V . In order to avoid any wall effects, periodic boundary conditions (PBC) are used. The RC particles themselves are represented by spheres with an additional degree of freedom σ , which is here the diameter of the particle. The Hamiltonian of this coarse-grained (CG) system can be described under the two-body approximation as [13]

$$H(\mathbf{r}^{N_{RC}}, \sigma^{N_{RC}}) \simeq F_0(N_{RC}, V) + \sum_i^{N_{RC}} \Psi(\sigma_i) + \frac{1}{2} \sum_{i \neq j} \phi(\mathbf{r}_i, \mathbf{r}_j, \sigma_i, \sigma_j). \quad (27)$$

The first term is the so-called volume term, which is independent of the configuration $\{\mathbf{r}_i, \sigma_i\}$ and includes the free energy of an isolated polymer, independent of its center of mass position [14]. The second term represents one-body energy changes connected to fluctuations in particles i 's property σ . Thus, $\Psi(\sigma_i)$ reflects a potential energy function of the property, defined by

$$\beta\Psi(\sigma) = -\ln p(\sigma). \quad (28)$$

Here, $\beta = \frac{1}{k_B T}$ is the inverse thermal energy, and $p(\sigma)$ is the property probability distribution function of a single responsive colloid particle. In the case where σ is the diameter of the particle, $p(\sigma)$ can be seen as the fluctuation in size around an equilibrium state σ_0 . The last term in eq. (27) represents the two-body pair potential. However, $\phi(\mathbf{r}_i, \mathbf{r}_j, \sigma_i, \sigma_j)$ is explicitly dependent on the position \mathbf{r}_i and the property σ_i . In our homogeneous system, the pair interaction $\phi(\mathbf{r}_i, \mathbf{r}_j, \sigma_i, \sigma_j) = \phi(r, \sigma_i, \sigma_j)$ depends only on the distance $r = |\mathbf{r}_i - \mathbf{r}_j|$. When using the low-density limit (LDL) relation [15]

$$\lim_{\rho_0 \rightarrow 0} g(r, \sigma_i, \sigma_j) = \exp[-\beta\phi(r, \sigma_i, \sigma_j)], \quad (29)$$

where $g(r, \sigma_i, \sigma_j)$ and ρ_0 are the normalized pair distribution function and the bulk density, as well as a coarse-grained pair potential

$$v(r) = -k_B T \ln(g(r)), \quad (30)$$

we can define the relation [15]:

$$\beta v(r) = -\ln \left(\int_{\Sigma} d\sigma_j p(\sigma_j) \int_{\Sigma} d\sigma_i p(\sigma_i) \exp[-\beta\phi(r, \sigma_i, \sigma_j)] \right). \quad (31)$$

Thereby, $v(r)$ is the conventional effective pair potential, which is usually acquired by integrating out the degree of freedom of the property in the low density limit.

4.2 Computational Model and Simulation Details

Because of their relatively small size, colloid particles in a liquid dispersion medium exhibit Brownian motion. As described in the previous chapter, our RC system is made up of $N_{\text{RC}} = 100$ sphere-like RC particles in a liquid. This means that we can simulate the particle dynamics using Brownian dynamics of motion. The whole system is in a canonical ensemble (NVT) with $k_B T = 1.0$, k_B being the Boltzmann constant, and T the temperature of the system. The volume V is a constant cube with periodic boundary conditions. The cube is defined over its side length l_{box} at the beginning of the simulation, depending on the chosen packing fraction η

$$l_{\text{box}}(\eta) = \left(\frac{4}{3} \pi R_0^3 N_{\text{RC}} / \eta \right)^{1/3}. \quad (32)$$

Here, the packing fraction is defined as

$$\eta = \frac{\frac{4}{3} \pi R_0^3 N_{\text{RC}}}{V} \quad (33)$$

with $R_0 = \sigma_0/2$ being the mean radius at the low-density limit at $\eta = 0.03$.

To keep particle dynamics simple, we ignore inertia and assume that the particle positions evolve according to a step-by-step scheme of Brownian dynamics, where motion is strongly slowed by friction [15]. With eq. (6), we can formulate a discretized equation of motion as:

$$\mathbf{r}_i(t + \Delta t) = \mathbf{r}_i(t) + \frac{D_T}{k_B T} \mathbf{F}_i(t) \Delta t + \boldsymbol{\xi}. \quad (34)$$

Here,

$$D_T = \frac{1}{\text{val}(\sigma_0)} \frac{\sigma_M^2}{\tau_{BD}} \quad (35)$$

is the translation diffusion coefficient. While σ_0 denotes the mean colloid size in the low-density limit, in units of σ_M , $\text{val}(\sigma_0)$ refers only to the numerical value of σ_0 . The simulation time step is set to $\Delta t = 5 \cdot 10^{-3} \tau_{BD}$. The Brownian time unit τ_{BD} is interpreted here as the time required for a colloid particle to diffuse over a distance σ_0 , thus defining the fundamental time scale of the simulation.

With the total potential energy of the system $U(\mathbf{r}^N(t), \sigma^N(t))$ following the Hamiltonian defined in eq. (27), we can calculate the translation force of the particle i as:

$$\mathbf{F}_i(t) = -\nabla_i U(\mathbf{r}^N(t), \sigma^N(t)) = -\sum_{j \neq i} \nabla_i \phi(\mathbf{r}_i, \mathbf{r}_j, \sigma_i, \sigma_j) \quad (36)$$

The last term $\boldsymbol{\xi}$ in the equation of motion represents the stochastic position update from Brownian motion. Each Cartesian component ξ_l ($l \in [x, y, z]$) of vector $\boldsymbol{\xi}$ is sampled from a normal distribution with mean $\langle \xi_l \rangle = 0$ and variance $\langle \xi_l^2 \rangle = 2D_T \Delta t$ and is strictly δ -correlated in time [15].

Now we also need an equation of motion for the extra degree of freedom of the property σ . Because we want a simple coarse-grained model, we assume overdamped dynamics for σ given by

$$\sigma_i(t + \Delta t) = \sigma_i(t) + \frac{D_\sigma}{k_B T} F_i^\sigma \Delta t + \xi_\sigma. \quad (37)$$

$D_\sigma = \frac{1}{\text{val}(\sigma_0)} \frac{\sigma_M^2}{\tau_{BD}}$ is here the property diffusion coefficient and ξ_σ represents stochastic noise drawn from a normal distribution with the mean $\langle \xi_\sigma \rangle = 0$ and the variance $\langle \xi_\sigma^2 \rangle = 2D_\sigma \Delta t$. The property force is calculated by the following method:

$$F_i^\sigma = -\frac{\partial U(\mathbf{r}^N(t), \sigma^N(t))}{\partial \sigma_i} = -\frac{\partial \Psi(\sigma_i)}{\partial \sigma_i} - \sum_{j \neq i} \frac{\partial}{\partial \sigma_i} \phi(\mathbf{r}_i, \mathbf{r}_j, \sigma_i, \sigma_j). \quad (38)$$

Here, it is important to note that the property force F_i^σ is not calculated solely on the basis of the property potential $\Psi(\sigma_i)$ but also from the interaction potential dependent on σ , $\phi(\mathbf{r}_i, \mathbf{r}_j, \sigma_i, \sigma_j)$.

We now conduct our simulations for a list of packing fractions between 0.03 and 4.01, in the same range as Del Monte and Zaccarelli [16] for later comparison. Thereby we start with an equilibration of the system for 10^7 time steps Δt . This is then followed by production runs of $2 \cdot 10^7$ time steps Δt for each packing fraction. To save computation time, the particles of a new production run begin at the last positions of the previous run and skip a new equilibration run. The position of the particle is saved for each 500 time step.

5 Results and Discussion

We begin by deriving a property potential $\Psi(\sigma)$ and a two-body interaction potential $\phi(r, \sigma_i, \sigma_j)$ from the low-density limit (LDL) of the simulation of the beads network (BN) by Del Monte and Zaccarelli[16]. Using these potentials, we then perform coarse-grained (CG) simulations with the previously presented CG responsive colloid model and subsequently present the resulting structural and thermodynamic properties.

5.1 Property Potential

The first step is to obtain a property potential $\Psi(\sigma)$ from the colloids in the BN simulation. Therefore, we take the emergent size distribution in the LDL, $\tilde{p}_{0.03}^{\text{BN}}(R_g)$, from Del Monte and Zaccarelli [16]. We then use eq. (26) to express the emergent size distribution as a function of the real diameter of the particle. In their simulations, the lowest packing fraction is $\eta = 0.03$. At this density, direct interactions between particles can be considered negligible due to the low concentration.

Throughout this thesis, the emergent size distribution provided by Del Monte and Zaccarelli will be denoted as $\tilde{p}_\eta^{\text{BN}}(\sigma)$, representing the recalculated distribution expressed in terms of the real particle diameter σ .

First, we must normalize the emergent size distribution, so

$$\int_{\Sigma} \tilde{p}_{0.03}^{\text{BN}}(\sigma) d\sigma = 1. \quad (39)$$

This normalization is performed for every emergent size distribution before further use.

This makes $\tilde{p}_{0.03}^{\text{BN}}(\sigma)$ a size probability distribution, allowing us to state that it is now the parent function $p(\sigma)$ of $\Psi(\sigma)$. With this and the relation eq. (28) we now have the property potential data $-k_B T \ln(\tilde{p}_{0.03}^{\text{BN}}(\sigma))$ from the BN simulation. In fig. 3, the crosses show the just calculated property potential values $-k_B T \ln \tilde{p}_{0.03}^{\text{BN}}(\sigma)$, shifted down so that the minimum lies at $0 k_B T$. This adjustment is valid because we are primarily interested in the resulting force, which is calculated from the derivative of Ψ .

The next step is to find a function that fits the data points. Upon examining the data again, we observe that the potential exhibits a parabolic shape with a minimum at approximately $44.5 \sigma_M$. In addition, there appears to be a small saddle point on the right tail at $\approx 49 \sigma_M$. We begin by fitting the area around the minimum with a polynomial of order two:

$$\Psi^{\min}(\sigma) = a_0(\sigma - \sigma_0)^2. \quad (40)$$

The fitted area around the minimum is shown in the top left plot of fig. 3. The resulting fitting parameters are presented in table 2. Examining $\Psi^{\min}(\sigma)$ in fig. 3 (dotted line), we see that it fits well around the minimum but diverges from the fit data on its

tails. Our next goal is to address the tails of the potential data. Therefore, we expand the fit function to a polynomial of order four, given by:

$$\Psi_4^{\text{poly}}(\sigma) = \Psi^{\text{min}}(\sigma) \cdot (b_0 + b_1\sigma + b_2\sigma^2). \quad (41)$$

Only the new parameters b_0 , b_1 and b_2 are now fitted over the entire potential data, while the initial determined parameters of $\Psi^{\text{min}}(\sigma)$ are retained. The resulting parameters can also be found in table 2. The parameter σ_0 now represents the equilibrium size of the colloidal particles in the most swollen state.

Upon reviewing fig. 3, we observe that $\Psi_4^{\text{poly}}(\sigma)$ now also covers the tails of the potential data. However, it diverges before and around the saddle point. In the region surrounding the minimum, shown on the bottom left plot, $\Psi_4^{\text{poly}}(\sigma)$ aligns well with the data, but weakens slightly for higher values of σ . This trend continues until $\sigma = 50\sigma_M$, at which point it effectively covers the tail.

Examining the area with smaller values of σ , we find that the potential energy is increasing continuously, surpassing $10^3 k_B T$ for $\sigma < 20\sigma_M$. $\Psi^{\text{min}}(\sigma)$ reaches around $10^2 k_B T$ at a similar particle size. A significant challenge arises from the fact that we only have data for the property potential between $38\sigma_M$ and $54\sigma_M$. We do not know what $\Psi(\sigma)$ looks like outside this range. In the BN simulation conducted by Del Monte and Zaccarelli, the shrinkage of the particles is a consequence of the increase in the packing fraction [16]. However, at higher packing fractions, where particle crowding increases, the particle interaction $\phi(r, \sigma_i, \sigma_j)$ begins to dominate. This complicates the use of the emergent size distribution at higher packing fractions to determine the pure property potential $\Psi(\sigma)$.

Table 2: Fit parameters for fitting $-k_B T \ln(\tilde{p}_{0.03}^{\text{BN}}(\sigma))$ using eq. (40) and eq. (41).

$a_0 [k_B T/\sigma_M]$	$s_0 [\sigma_M]$	b_0	$b_1 [1/\sigma_M]$	$b_2 [1/\sigma_M^2]$
0.1740 ± 0.0014	44.494 ± 0.005	20.5 ± 1.7	-0.79 ± 0.07	0.0078 ± 0.0008

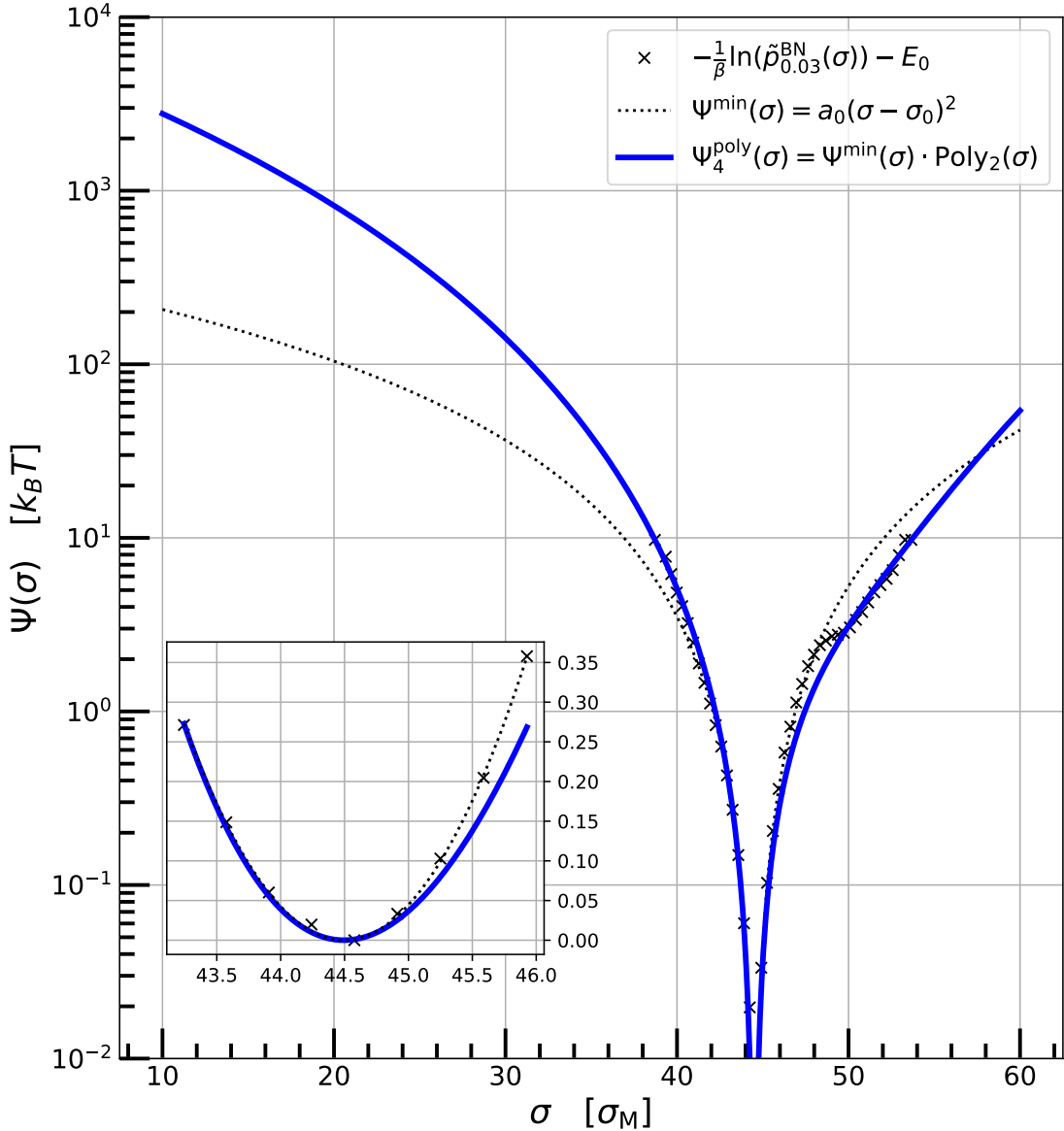


Figure 3: The black crosses represent the property potential $\Psi(\sigma) = -k_B T \ln(\tilde{p}_{0.03}^{BN}(\sigma))$ of the BN system in the LDL, calculated from the emergent size distribution $\tilde{p}_{0.03}^{BN}(\sigma)$ provided by Del Monet and Zaccarelli [16]. The dotted line shows the fit function $\Psi^{\min}(\sigma)$ (eq. (40)), fitted directly on the data around the minimum, as depicted in the bottom left plot. $\Psi_4^{\text{poly}}(\sigma)$ (blue line) is an expansion of $\Psi^{\min}(\sigma)$ to order four, fitted to the entire data set, while retaining the parameters of $\Psi^{\min}(\sigma)$.

5.2 Interaction Potential

The next step is to find an interaction potential $\phi(r, \sigma_i, \sigma_j)$ that describes the particle-particle interaction of the CG system of Del Monte and Zaccarelli. Therefore, we use the relation in eq. (31) and test different interaction potentials $\phi(r, \sigma_i, \sigma_j)$ until we find one that matches the effective potential v_{eff} of the BN system in the low density limit

(LDL).

The effective potential of the BN system is calculated from the radial distribution function $g_{0.03}^{\text{BN}}(r)$ in the LDL ($\eta = 0.03$) via eq. (30). The black dashed line in fig. 4 shows the calculated effective potential of the BN system. It can be observed that this potential decays towards zero at approximately $45 \sigma_M$, which is around the equilibrium particle size in the LDL, σ_0 , which we identified previously by fitting the property potential $\Psi(\sigma)$.

To begin, we fit a simple Hertzian potential (HZ) to the effective potential in the LDL obtained from the BN simulations using the formula provided in eq. (7). The fitting is performed with ϵ as the free parameter and fixed diameters $\sigma_{i/j} = \sigma_0$. The blue line in fig. 4 represents the fitted HZ potential $\phi_{\text{HZ}}^{\text{fit}}(r, \epsilon_{\text{fit}})$, with

$$\epsilon_{\text{fit}} = (108.7 \pm 0.2) k_B T. \quad (42)$$

For small sigma values, the fit follows the trend of the effective potential $v_{\text{eff}}(r) = -k_B T \ln(g_{0.03}^{\text{BN}}(r))$, however, at larger sizes it decreases more rapidly towards zero. Nevertheless, the effective potential is still reasonably well-described in a HZ like form. Therefore, we employ the HZ potential as the interaction potential $\phi(r, \sigma_i, \sigma_j)$, which is also typically used for non-responsive CG colloidal particle simulations. With this base form for the two-body interaction, along with the fitted property potential $\Psi_4^{\text{poly}}(\sigma)$ and the relation in eq. (28) for the parent function $p_4^{\text{poly}}(\sigma)$, we can calculate the effective potential through the relation in eq. (31).

For the interaction potential $\phi(r, \sigma_i, \sigma_j)$, we consider the size dependency of the interaction strength $\epsilon(\sigma_i, \sigma_j)$, as shown in eq. (9). However, this introduces a dependency on the Young modulus $Y(\sigma_{i/j})$ and the Poisson ratio $\nu(\sigma_{i/j})$ (see eq. (8)). For the Young modulus, we can use eq. (18) to calculate it as

$$Y(\sigma_i, c) = \frac{c}{\sigma_i^3}. \quad (43)$$

Here, c is a proportionality constant that relates Young's modulus Y of a colloidal particle to the inverse cube of its size σ_i . For the Poisson ratio, we consider a constant value of $\nu = 0.3$. This choice is based on simulations by Rovigatti *et al.* [28] for swollen microgels similar to those used in the BN system [16]. They showed that the Poisson ratio ν lies between 0.25 and 0.3 for swollen microgels with cross-link concentrations similar to the BN model. This is also in agreement with experiments that determine ν between 0.3 and 0.4 for swollen microgels [10, 11].

With the now-defined values for the Young modulus Y , Poisson ratio ν and the equations from eq. (7) to 10, we can define a HZ potential of the form:

$$\phi_c(r, \sigma_i, \sigma_j) = \epsilon(\sigma_i, \sigma_j, c) \left(1 - \frac{r}{\sigma_{ij}}\right)^{5/2} \Theta\left(1 - \frac{r}{\sigma_{ij}}\right), \quad (44)$$

$$\epsilon(\sigma_i, \sigma_j, c) = \frac{8}{15} A_{\text{eff}}(\sigma_i, \sigma_j, c) \left(\frac{\sigma_i + \sigma_j}{2}\right)^2 \left(\frac{\sigma_i \sigma_j}{4}\right)^{1/2}, \quad (45)$$

$$A_{\text{eff}}(\sigma_i, \sigma_j, c) = \frac{A(\sigma_i, c) A(\sigma_j, c)}{A(\sigma_i, c) + A(\sigma_j, c)}, \quad (46)$$

$$A(\sigma_{i/j}, c) = \frac{Y(\sigma_{i/j}, c)}{1 - \nu^2}, \quad (47)$$

$$Y(\sigma_{i/j}, c) = \frac{c}{\sigma_{i/j}^3} \quad \& \quad \nu = 0.3. \quad (48)$$

With c as a free parameter, we can now calculate the effective potential using eq. (31). Through trial and error, we set $c = 750 k_B T$. The resulting effective potential is shown as the orange line in fig. 4. It exhibits behavior similar to that of the BN model for small diameters, while decreasing slightly faster for larger diameters. However, in general, it provides a good description of the effective potential of the BN model in the LDL.

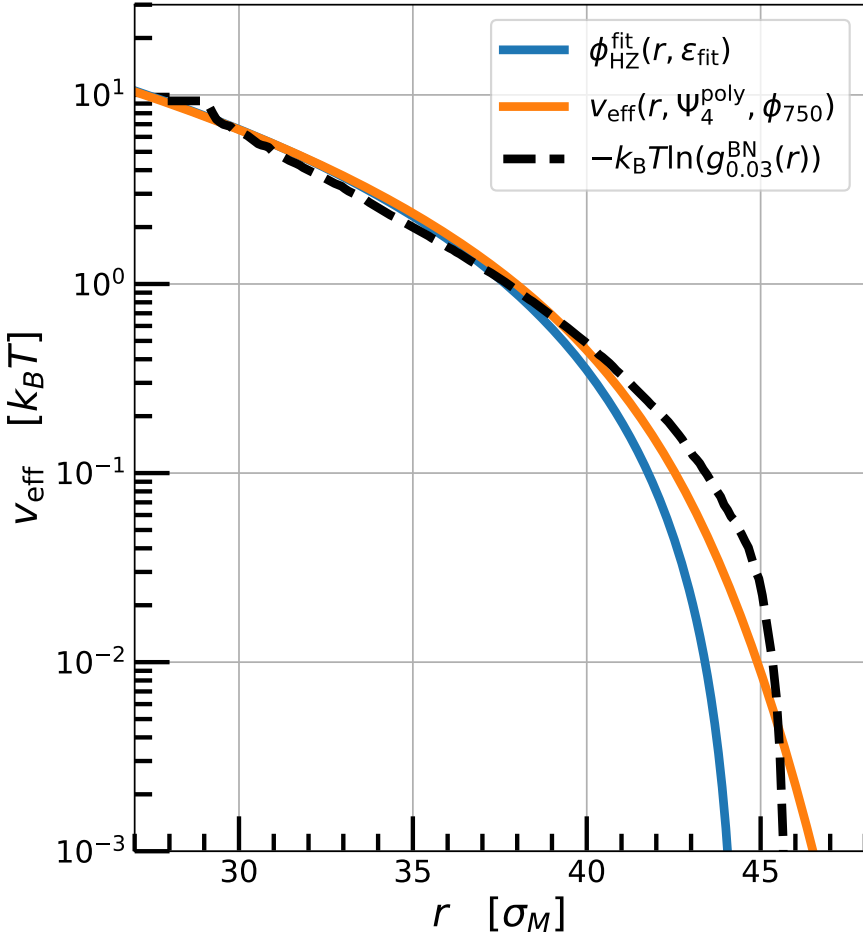


Figure 4: The dashed line shows the effective potential in the LDL of the BN simulation calculated from the radial distribution function $g_{0.03}^{BN}(r)$ from Del Monte and Zaccarelli [16]. The blue line represents a Hertzian potential fitted to the effective potential of the BN model, with the interaction strength ϵ as a fitting parameter. The orange line shows an effective potential calculated from eq. (31), using $p_4^{poly}(\sigma)$ and $\phi_{750}(r, \sigma_i, \sigma_j)$.

5.3 Emergent Size Distribution

With the property potential $\Psi_4^{poly}(\sigma)$ and the interaction potential $\phi_{750}(r, \sigma_i, \sigma_j)$, we can perform simulations as described in section 4.2. This section discusses the resulting emergent size distributions.

We start by examining some snapshots of our CG simulation. Figure 5 displays five different snapshots, ranging from the lowest packing fraction $\eta = 0.03$ to the highest packing fraction $\eta = 4.01$, along with their particle sizes indicated through a color bar on the bottom right corner. The first snapshot at $\eta = 0.03$ shows that all RC particles move freely within the simulation box. As the packing fraction increases, the particles become more crowded and form a large cluster. At $\eta = 0.87$, the cube appears nearly

completely filled with particles, and the first clear size adjustments are evident through the color change. The subsequent shown snapshot at $\eta = 2.52$ reveals a noticeable shrinkage of all particles, and some kind of arrangement in their positions. Finally, at the highest packing fraction, we observe a more chaotic order, as well as further size reduction. Overall, we conclude that our system responds to increasing packing fractions with greater crowding and size adjustments as the particles come into contact.

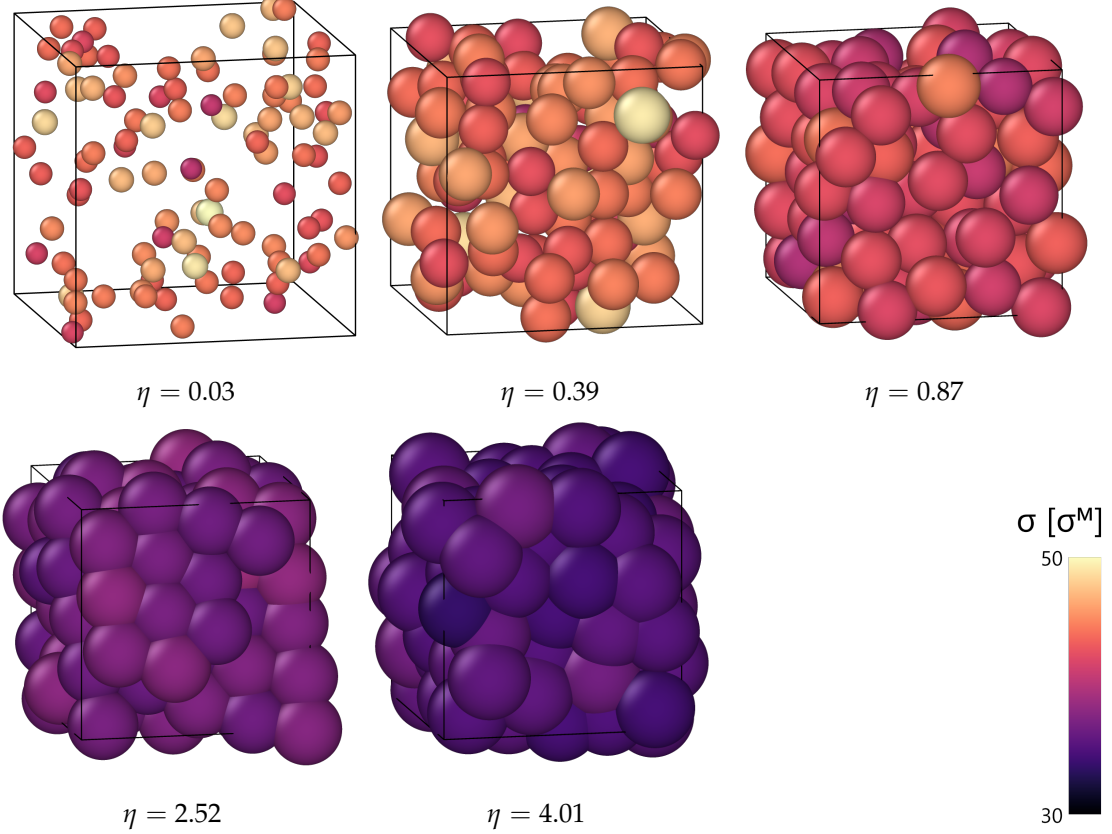


Figure 5: Representative snapshots of the coarse-grained responsive colloidal particles, with the property potential $\Psi_4^{poly}(\sigma)$, at packing fractions $\eta = 0.03, 0.39, 0.87, 2.52$ and 4.01 from left to right. The particle size is represented by the color of the spheres, as defined by the color bar on bottom right corner.

If we now compare our snapshots to those from Del Monte and Zaccarelli, in fig. 6, we can clearly observe the different levels of coarse-graining in both models. In our RC model, the particles are represented as simple spheres with an additional degree of freedom, while in the BN model, they consist of thousands of connected "beans". Both cases exhibit shrinking behavior with increasing packing fraction. However, simulation particles in the BN model respond to close packing not only with volume changes but also with alterations in their general shape and interpenetration with other particles [16].

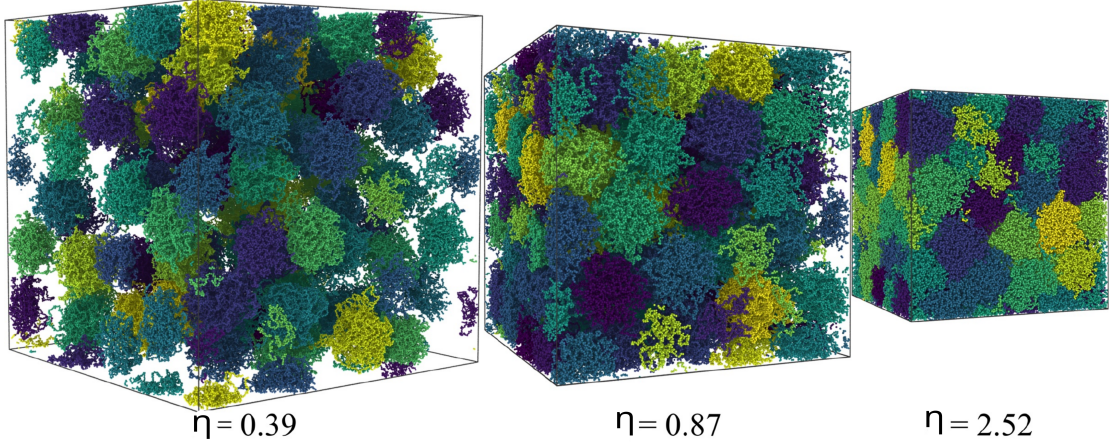


Figure 6: Reproduction of fig. 2 for comparison to fig. 5. Here the different colors only separate different particles. Snapshots of the BN system at different packing fractions ζ . Originally taken from [16].

Next, we take a closer look at the shrinking behavior of the colloids by interpreting their emergent size distributions $\tilde{p}_\eta(\sigma)$. These distributions are obtained by binning all particle sizes across all time steps into a histogram, from which we extract the bin centers as x -values and their frequencies as y -values. The data is then normalized so that $\int y \, dx = 1$, resulting in a probability density function. The resulting distributions $\tilde{p}_\eta(\sigma)$ are presented in fig. 7 for all simulated packing fractions. We observe a clear shift towards smaller particle diameters σ with an increasing packing fraction η . Focusing first on the low- η cases, we find no size changes between the two lowest packing fractions and only a small drift toward lower diameters until $\eta = 0.50$. This directly indicates little to no particle interaction at low packing fractions η . As we move to packing fractions of $\eta > 0.50$, the size distributions show a much clearer shift towards smaller diameters σ . We also notice that $\tilde{p}_\eta(\sigma)$ is becoming leaner with increasing packing fraction, especially visible at high η values. This suggests a narrowed size fluctuation in crowded systems. The height increase of the distributions is a result of the normalization due to their thinning. In general, we observe particle deswelling and reduced size fluctuations with increasing packing fraction η in our system. The findings align with other CG responsive simulations [15, 18] and are consistent with experimental observations [6, 8].

Now we compare the size development with increasing packing fraction in our CG simulation with the BN model of Del Monte and Zaccarelli [16]. To do this, we first calculate the mean particle diameter $\langle \sigma \rangle$ and the variance $\langle \sigma^2 \rangle - \langle \sigma \rangle^2$ from the normalized emergent size distributions $\tilde{p}_\eta(\sigma)$ and $\tilde{p}_\eta^{\text{BN}}(\sigma)$, using

$$\langle \sigma \rangle = \int_{\Sigma} \sigma \tilde{p}_\eta(\sigma) \, d\sigma, \quad (49)$$

$$\langle \sigma^2 \rangle - \langle \sigma \rangle^2 = \int_{\Sigma} (\sigma - \langle \sigma \rangle)^2 \tilde{p}_\eta(\sigma) \, d\sigma. \quad (50)$$

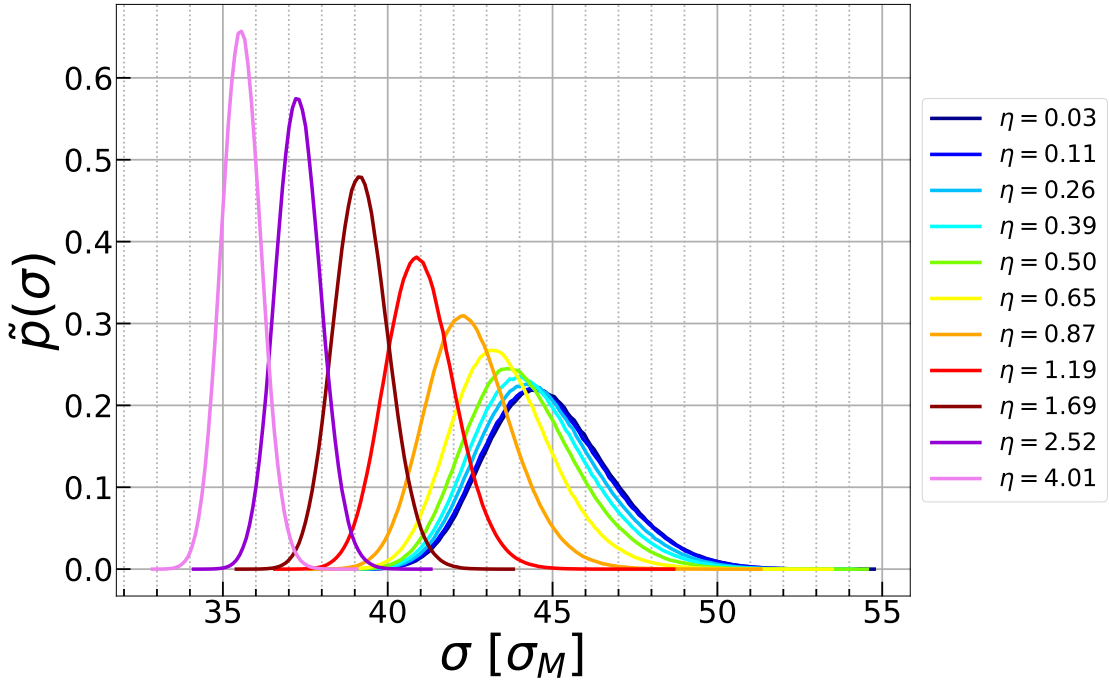


Figure 7: Emergent size distributions $\tilde{p}_\eta(\sigma)$, of the CG model with the property potential $\Psi_4^{poly}(\sigma)$ for increasing packing fractions η from right to left.

The mean particle sizes determined, depending on the packing fraction of their size distributions, are presented in fig. 8(a). We start by examining the low η region, where we see that $\langle \sigma \rangle$ remains approximately constant in both cases. Between $\eta \simeq 0.5$ and $\simeq 1.0$, both mean particle diameters start to shrink slowly, with our CG simulation exhibiting a slightly stronger decrease. Around $\eta = 1.0$, both simulations show clear shrinking behavior with increasing packing fractions. However, in our CG simulation, the responsive colloidal particles shrink only to a mean diameter of $\langle \sigma \rangle_{4.01} \approx 35.5 \sigma_M$ at the highest packing fraction $\eta = 4.01$. In comparison, the mean diameters of the BN model shrink below $30 \sigma_M$ at the same packing fraction, indicating that the particles in the BN system demonstrate stronger deswelling behavior than our CG particles.

The dashed line in fig. 8(a) represents isotropic shrinking, corresponding to a uniform contraction of the particles in all spatial directions as the density increases. We can theoretically derive this behavior using the definitions of the packing fraction η (eq. (33)) and the effective packing fraction η_{eff} :

$$\eta = \rho \frac{\pi}{6} \sigma_0^3 \quad \Rightarrow \quad \eta \propto \rho \quad (51)$$

$$\eta_{\text{eff}} = \rho \frac{\pi}{6} \langle \sigma(\eta) \rangle^3 \quad \Rightarrow \quad \langle \sigma(\eta) \rangle^3 \propto \frac{1}{\rho} \quad \text{or} \quad \langle \sigma(\eta) \rangle \propto \rho^{-1/3} \quad (52)$$

$$\Rightarrow \quad \langle \sigma(\eta) \rangle \propto \eta^{-1/3}. \quad (53)$$

Here, $\rho = \frac{N}{V_{\text{box}}}$ is the number density.

Since we aim for behavior similar to that observed in the BN model, we use their data to calculate the reference for isotropic shrinking. The scaling in eq. (53) holds only if $\eta_{\text{eff}} \approx \text{constant}$. Although Del Monte and Zaccarelli [16] report that their particle shrinkage is compatible with isotropic shrinkage, their effective packing fraction does not reach a constant regime. Nevertheless, for our purpose, we assume that at the highest packing fraction $\eta = 4.01$, η_{eff} is approximately constant and calculate the expected isotropic shrinkage as

$$\langle \sigma \rangle_{\text{iso}} = \sigma_{\text{ref}} \left(\frac{\eta_{\text{ref}}}{\eta} \right)^{1/3}, \quad (54)$$

where σ_{ref} is the mean particle diameter at the reference packing fraction $\eta_{\text{ref}} = 4.01$. Since we assume isotropic shrinkage only after full particle contact, the reference line starts at $\eta = 1$. When comparing the trend of our mean diameters at high packing fractions with the isotropic shrinking reference curve, we observe that the decrease is less steep. Although our CG colloidal particles can only shrink uniformly over their diameters, the system does not exhibit isotropic shrinking at high densities. This difference comes from the property potential $\Psi_4^{\text{poly}}(\sigma)$ becoming too strong in this regime, effectively preventing further shrinking. In addition, the soft nature of the Hertzian interparticle interaction allows the particles to overlap instead of continuing their shrinkage, leading to an additional less decrease in the mean particle diameter.

Looking at fig. 8(b), we observe the variances of the emergent size distributions $\tilde{p}_\eta(\sigma)$. While in the BN model $\langle \sigma^2 \rangle - \langle \sigma \rangle^2$ remains approximately constant until $\eta \rightarrow 1.0$, the variance in our CG system drops directly for $\eta > 0.1$. However, both systems generally exhibit a similar decrease in the variation of accessible particle sizes with increasing packing fraction.

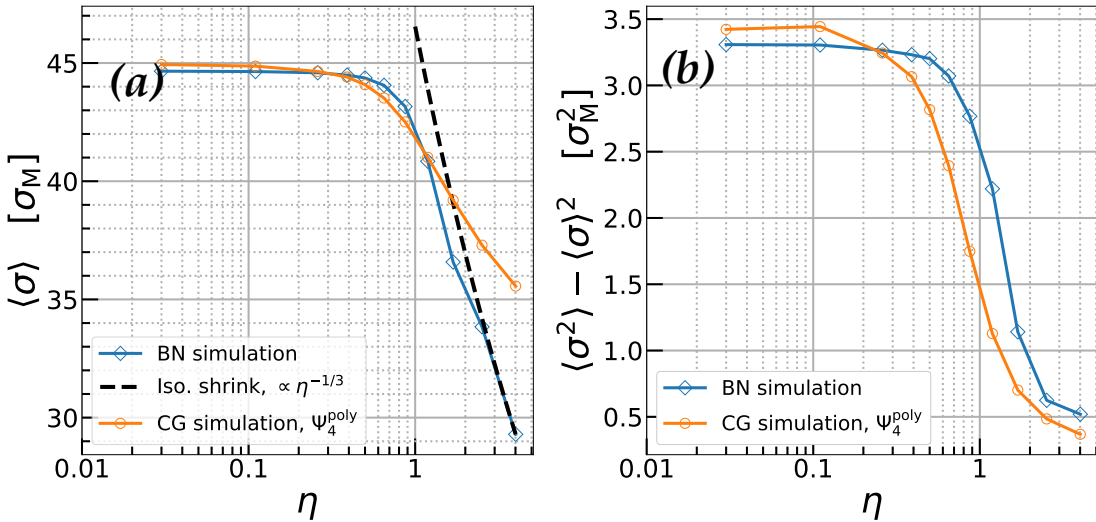


Figure 8: Mean particle sizes (a) and variance (b) calculated using eq. (50) from $\tilde{p}_\eta(\sigma)$ and $\tilde{p}_\eta^{\text{BN}}(\sigma)$. Here, $\tilde{p}_\eta(\sigma)$ is determined from the particle sizes of our CG model with the property potential $\Psi_4^{\text{poly}}(\sigma)$ and $\tilde{p}_\eta^{\text{BN}}(\sigma)$ is provided by Del Monte and Zaccarelli [16].

Because we observe particle shrinking with increasing density, the normal packing fraction η , calculated using the equilibrium particle size σ_0 in the most diluted state, no longer accurately reflects the true volume fraction of the particles. A better approach for this is the so-called effective packing fraction η_{eff} . It uses the actual particle size to determine the volume occupied by the particles. In our case, we use the previously determined mean particle diameter $\langle \sigma \rangle_\eta$ for each state, resulting in

$$\eta_{\text{eff}} = \frac{\frac{4}{3}\pi \left(\frac{\langle \sigma \rangle_\eta}{2}\right)^3 N_{\text{RC}}}{V(\eta)}. \quad (55)$$

Figure 9 presents the effective packing fraction η_{eff} as a function of η (blue line). The orange dotted line represents the case $\eta_{\text{eff}} = \eta$, characterizing a region with negligible particle shrinkage. We observe that the effective packing fraction follows this linear behavior until $\eta \approx 0.60$, indicating minimal particle interaction in that region and almost non-responsive behavior. Beyond this point, the two begin to differ, with η_{eff} increasing at a much slower rate. This suggests that at higher packing fractions, particle interaction starts to dominate, resulting in particle deswelling to counter overlaps. At $\eta \approx 1.30$, the effective packing fraction reaches $\eta_{\text{eff}} = 1.0$. Above this point, particles must overlap to compensate for the total particle volume being larger than the simulation box. The non-response area $\eta_{\text{eff}} = \eta$ at low packing fractions and the less steep rise in η_{eff} afterwards are also reported in other simulations [16, 18].

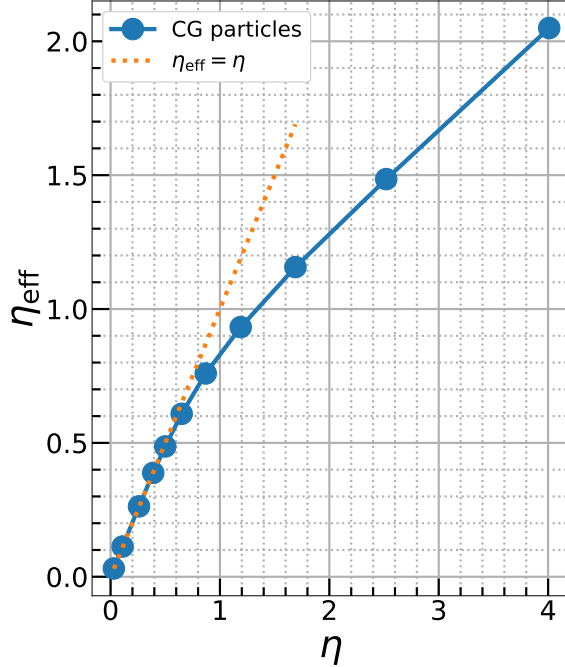


Figure 9: Effective packing fraction η_{eff} of our CG responsive model with property potential $\Psi_4^{\text{poly}}(\sigma)$, as a function of the packing fraction η . η_{eff} is calculated from the mean particle size $\langle \sigma \rangle_\eta$. The dotted line represents $\eta_{\text{eff}} = \eta$, indicating the case of a non responsive system.

5.4 Bulk Modulus

Bulk Modulus of Individual Particles

We start by taking a look at the bulk modulus of individual RC particles K_p . It is calculated by dividing the mean particle volume $\langle V \rangle$ by the volume variance $\langle V^2 \rangle - \langle V \rangle^2$ (see eq. (15)). To obtain these two quantities, we use our normalized size distribution $\tilde{p}_\eta(\sigma)$ and $V = \frac{\pi}{6}\sigma^3$, resulting in

$$\langle V \rangle = \int_{\Sigma} \tilde{p}_\eta(\sigma) \frac{\pi}{6} \sigma^3 d\sigma, \quad (56)$$

$$\langle V^2 \rangle - \langle V \rangle^2 = \int_{\Sigma} \tilde{p}_\eta(\sigma) \left(\frac{\pi}{6} \sigma^3 - \langle V \rangle \right)^2 d\sigma. \quad (57)$$

Using these formulas, we can now calculate K_p for different packing fractions η . The results are presented in (a) of fig. 10 together with the bulk moduli of individual particles of the BN system taken from Del Monte and Zaccarelli [16]. We observe that our CG system's K_p is roughly one order of magnitude smaller than that of the BN system. Although Del Monte and Zaccarelli also compute their K_p from volume fluctuations, they use a surface mesh on the individual colloidal particles to determine the volume. This approach enables them to capture deformations of the network, such as non-spherical shapes. As a result, their volume fluctuations reflect the mechanical response of the internal bead-chain structure. In contrast, our CG system only accounts for spherical volume changes and therefore does not capture internal deformation modes. In addition, already small changes in diameter lead, with $V \propto \sigma^3$, to a significant increase in volume. This increases the volume variance in our CG case and further contributes to the low K_p values.

Since we still want to compare the bulk modulus of individual particles, we recalculate K_p for the BN system using their size distributions $\tilde{p}_\eta^{\text{BN}}(\sigma)$, along with our formula for mean volume and variance eq. (57). In this way, the BN system now also accounts for spherical volume changes. The recalculations are represented by the green curve in fig. 10. As we can see, now both curves are in the same order of magnitude. At low packing fraction η both curves start at approximately the same level. As η increases, the two curves also rise in K_p , with our CG system showing a slightly steeper increase. This trend continues until $\eta = 2.5$, at which the BN model catches up and both converge around the same value. Generally speaking, the bulk modulus of individual particles K_p exhibits similar behavior in both systems as the packing fraction increases, assuming that we calculate K_p for the BN system based on changes in spherical volume.

Pressure and Bulk Modulus of the system

We continue with the bulk modulus of the whole system K . This is calculated directly from the derivation of pressure according to the volume (eq. (14)). The pressure of the system is thereby calculated throughout the simulation run for each packing fraction η using the virial equation (eq. (13)). In fig. 11 (a) the pressure P is shown as a function

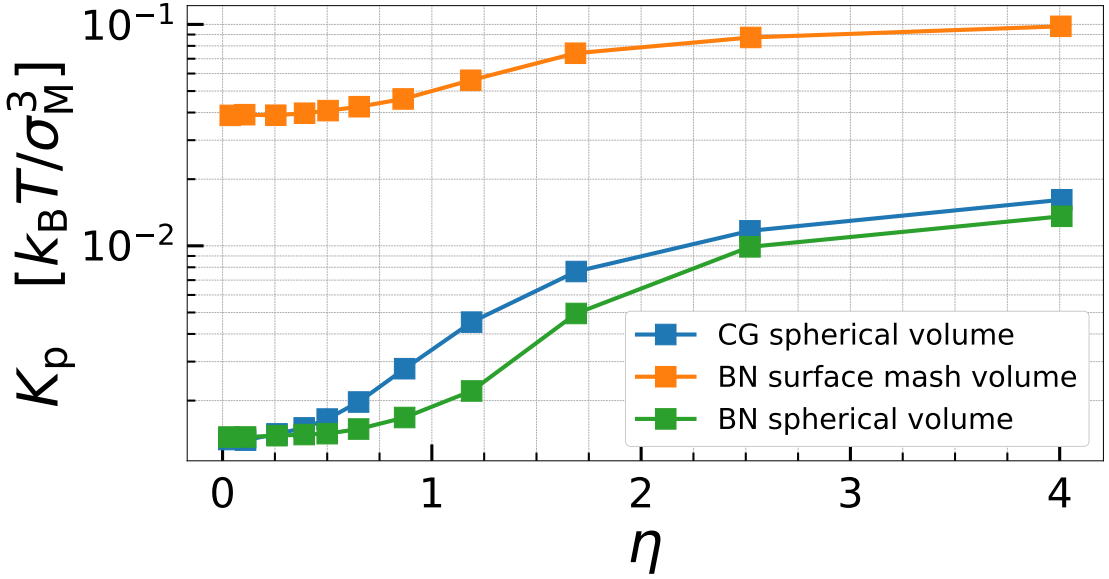


Figure 10: The Bulk modulus of individual particles K_p is calculated from spontaneous volume fluctuations eq. (15) and depends on the packing fraction η . The orange line represents the K_p of the BN system, calculated by Del Monte and Zaccarelli [16], which use a surface mesh to determine the volume. The green line shows K_p of the BN system, here we use the emergent size distribution $\tilde{p}_\eta^{\text{BN}}(\sigma)$ provided by Del Monte and Zaccarelli [16] to recalculate the particle volumes (assuming spherical volumes). The blue line reports on K_p of our CG system with the property potential $\Psi_4^{\text{poly}}(\sigma)$, for which we also employ the emergent size distribution $\tilde{p}_\eta(\sigma)$ for the volume calculations.

of the volume of the simulation box V . Because $V \propto 1/\eta$, the highest volume belongs to the lowest packing fraction $\eta = 0.03$ and the lowest volume to the highest packing fraction $\eta = 4.01$. With this we can see that the pressure decreases with the system volume, but increases with the packing fraction. So, a more crowded system results in an increase in pressure. Next, we calculate the bulk modulus K using a numerical derivation

$$K = -V \frac{\partial P}{\partial V} \approx -\frac{V_1 + V_2}{2} \cdot \frac{P_2 - P_1}{V_2 - V_1} \quad (58)$$

Figure 11 (b) shows the calculated bulk modulus for our CG system and the one for the BN system of Del Monte and Zaccarelli[16]. We observe a significant difference between the two curves, with K from the BN system being much larger than in our case. At low packing fractions η , both systems show a small bulk modulus, as expected when there is almost no particle interaction. However, K from the BN is already larger than in our CG case. This difference only increases with larger packing fractions. While our system reaches some kind of plateau at around $K = 7 \cdot 10^{-3} k_B T / \sigma_M^3$, the BN system climbs to approximately $4 k_B T / \sigma_M^3$. The reason for this could again be the different inner particle structures in the two systems. In the BN system, at high packing fractions, the colloidal particles are densely packed. This results in complex many-body interactions between chains within the same particle or with neighboring particles. This makes the whole system much more resistant to compression. On the

other hand, in our CG system, the particles can freely overlap due to the soft nature of the HZ potential if they lack space, making the system itself more soft and resulting in a smaller bulk modulus K .

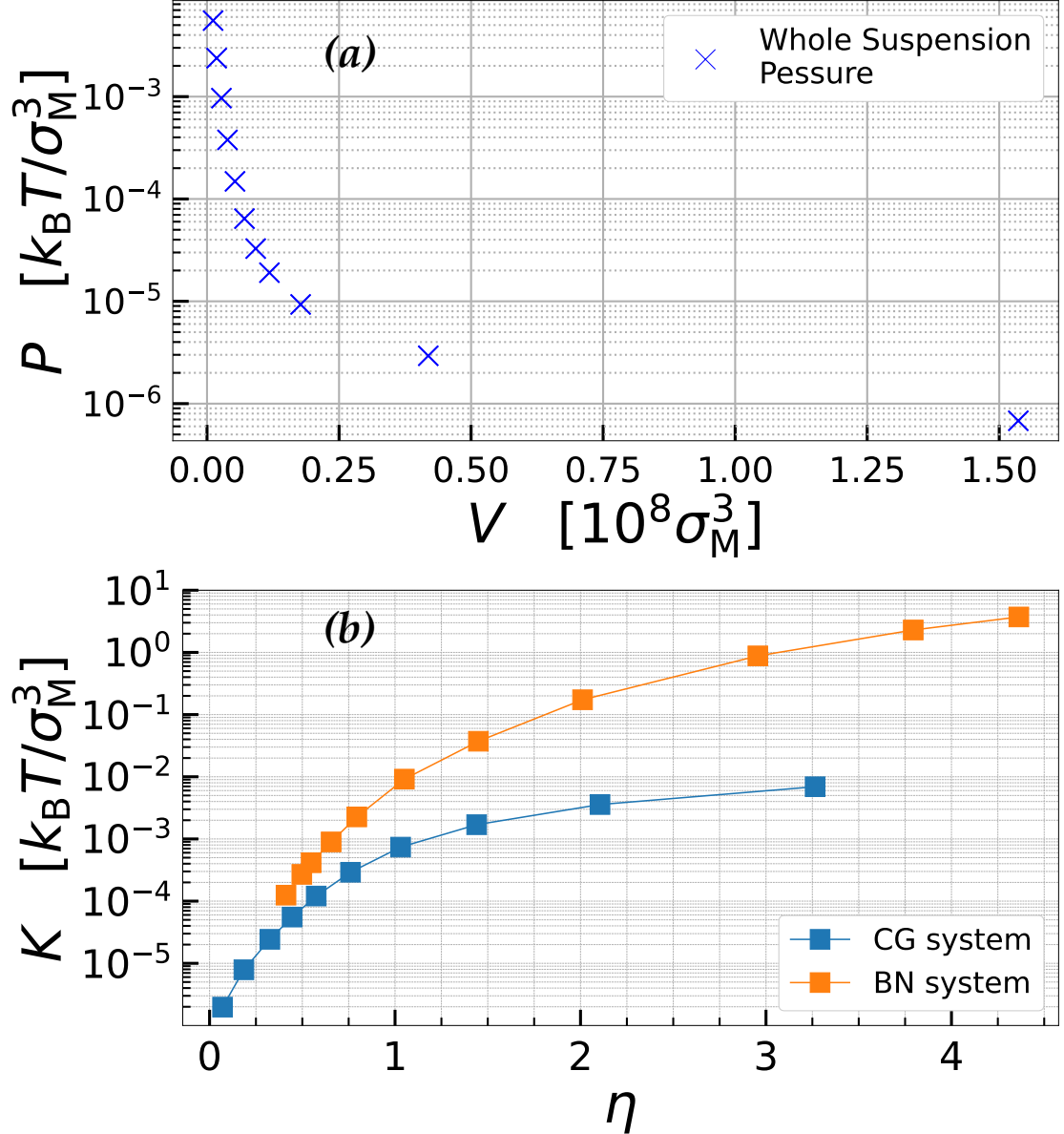


Figure 11: (a): System pressure P of our CG model with the property potential $\Psi_4^{poly}(\sigma)$, calculated using the virial equation (eq. (13)).
(b): Bulk modulus of the whole system K , calculated directly from the derivation of pressure according to the volume. The orange line shows K from the BN system calculated by Del Monte and Zaccarelli [16]. The blue line presents K from our CG system with property potential $\Psi_4^{poly}(\sigma)$, calculated from eq. (58).

5.5 Radial-Distribution Function

Next, we take a closer look at the collective properties of the whole system, starting with the radial distribution function (RDF) $g(r)$. These are thereby calculated from the positions of the particles with eq. (20). $g(r)$ is reported in fig. 12 as a function of the packing fraction η . At the lowest packing fraction $\eta = 0.03$ we can see that the RDF does not have a main peak and goes directly to $g(r) \approx 1.0$. This indicates that there is no real particle structure or interaction comparable to that of an ideal gas. At higher packing fraction η , the resulting $g(r)$ curves show the appearance of a main peak. The main peak $g(r_{\max})$ of the RDF increases in height, and its position r_{\max} gradually shifts to smaller distances r for larger packing fractions η . This trend implies stronger interparticle correlations and the emergence of short-range structural arrangements. The process reaches its climax at the value $\eta = 1.69$ with a maximum $g(r_{\max}) \approx 3.4$. Beyond this point, we can observe a decrease in $g(r_{\max})$ with an especially large drop in $\eta = 4.01$. Here, the main peak drops again below a value of two and becomes broader and less well-defined. This indicates that at excessive particle crowding the particle overlapping gets significant, leading to less structural order. The shift to smaller distances r and the re-entrant behavior of the main peak $g(r_{\max})$ with increasing packing fraction η is also visible in other computer simulations[16, 18] as well as in experimental measurements[7].

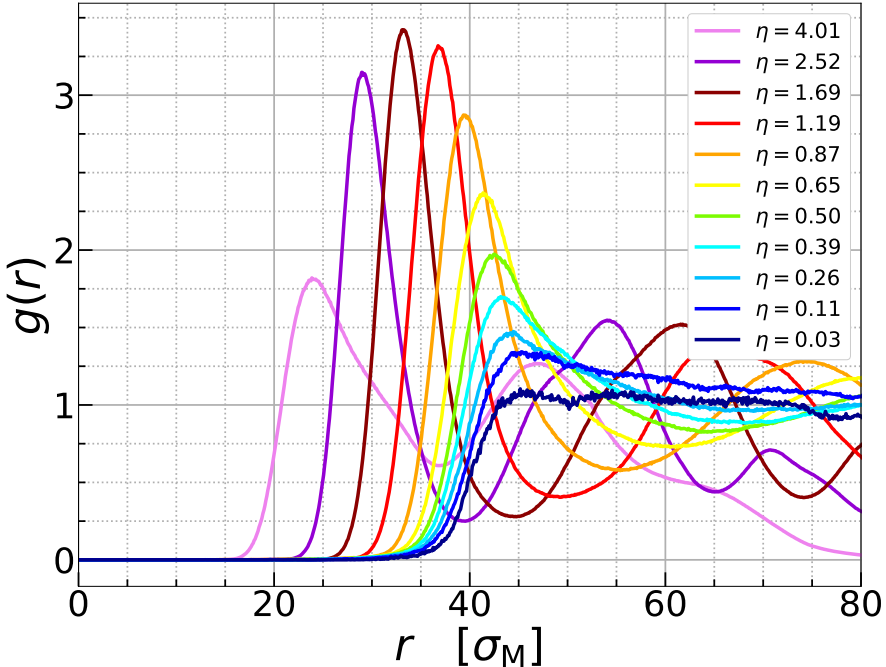


Figure 12: Radial distribution function of the CG model with property potential $\Psi_4^{poly}(\sigma)$, for different packing fractions η .

Now we compare the RDF of our CG system with those obtained by Del Monte and Zaccarelli[16]. In addition, we perform a non-responsive CG simulation, using only a

simple Hertzian potential(eq. (7)) with no property potential Ψ and a constant particle size σ_0 from table 2. For the interaction strength, we use $\epsilon = 470 k_B T$, also used by Del Monte and Zaccarelli for their non-responsive model [16]. We start with fig. 13(a) that shows the position of the main RDF peak as a function of the packing fraction η . There we can see a clear shift to shorter distances r_{\max} with increasing η in all three cases. The distance r_{\max} of our CG responsive simulation always lies a few σ_M above the corresponding distances of the BN system, except for the two lowest packing fractions where it is the other way around. For lower packing fractions, the non-responsive CG simulation shows distances similar to the responsive one, before dropping near the BN system for high η .

Now we examine the main peak height $g(r_{\max})$ shown in fig. 13(b). In all three cases, $g(r_{\max})$ initially increases with the packing fraction η before again decreasing for high values of η . Both the BN and the non-responsive simulations reach their maximum value for $g(r_{\max})$ at the same packing fraction, $\eta = 0.89$. In contrast, our CG responsive simulation reaches its maximum later at $\eta = 1.69$. The maximum peak heights also differ: the BN system reaches $g(r_{\max}) \approx 4$, the non-responsive system reaches $g(r_{\max}) \approx 5.2$, and the CG responsive system only reaches $g(r_{\max}) \approx 3.4$. This suggests that the isotropic shrinkage of the individual CG particles in our model delays structural ordering and limits peak height compared to other models, by creating more free volume.

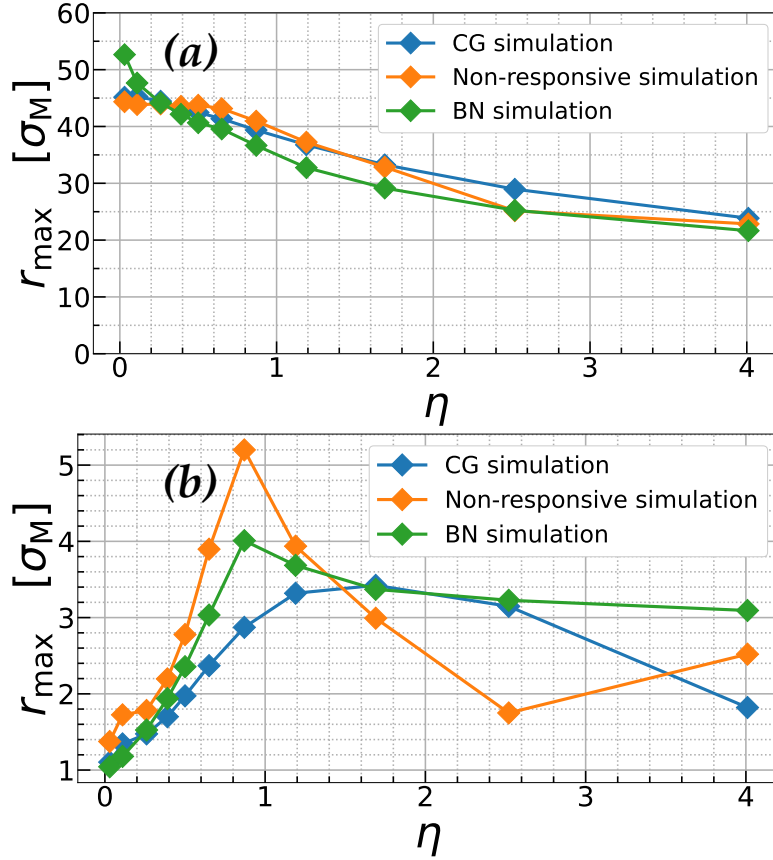


Figure 13: Main RDF peak position **a)** and peak height **(b)** as a function of the packing fraction η for different simulation models. The RDF values from the BN model come from Del Monet and Zaccarelli [16]. The CG simulation refers to our CG responsive model with property potential $\Psi_4^{\text{poly}}(\sigma)$ and the non-responsive simulations are based on a simple CG model with constant particle size and a simple Hertzian potential (eq. (7)) with $\epsilon = 470 k_{\text{B}}T$ [16].

5.6 Mean Squared Displacement

At last, we examine the mean squared displacement (MSD) as defined in eq. (23). To do this we first need to unwrap the particle positions from the used periodic-boundary condition to get the actual traveled distances of our particles. The then determined MSDs are shown in fig. 14 for different packing fractions as a function of time.

For low packing fractions up to approximately $\eta = 0.50$, the system reaches a diffusive regime, as indicated by the MSD curves having a slope close to one. With increasing packing fractions, the curves become more shallow at long times, reflecting a slowdown in particle movement due to enhanced crowding and caging effects. This slowdown trend reaches its maximum around $\eta > 1.69$, where we can observe an apparent plateau region between $t = 10^3 \tau_{\text{BD}}$ and $10^4 \tau_{\text{BD}}$, indicating a temporary freeze in movement and a glass-like state of the system. However, this behavior changes for longer times, where the MSD curves rise again, suggesting a regaining in particle movement and a structural rearrangement within the whole system. This trend is most

pronounced at the highest packing fraction $\eta = 4.01$, where the motion again becomes diffusive. This regained particle mobility at high densities can be traced back to the soft nature of the Hertzian potential, which allows particle overlapping resulting in a re-entrant in a fluid-like state. The observed plateau for high packing fraction is similar to the MSD measurements done in experiments [12].

Figure 15 shows the MSD curves of the BN model, obtained by Del Monte and Zaccarelli[16]. For $\eta < 0.87$ the particles reach a diffusive regime at long times. At higher packing fractions, we can observe the curves becoming more shallow, indicating a slowdown in particle dynamics. In contrast to our CG model, the BN model does not exhibit a revival in particle mobility, but instead shows a continuous slowdown, illustrating transitions towards a glass-like state. This again suggests that our current model reacts much softer to dense packing.

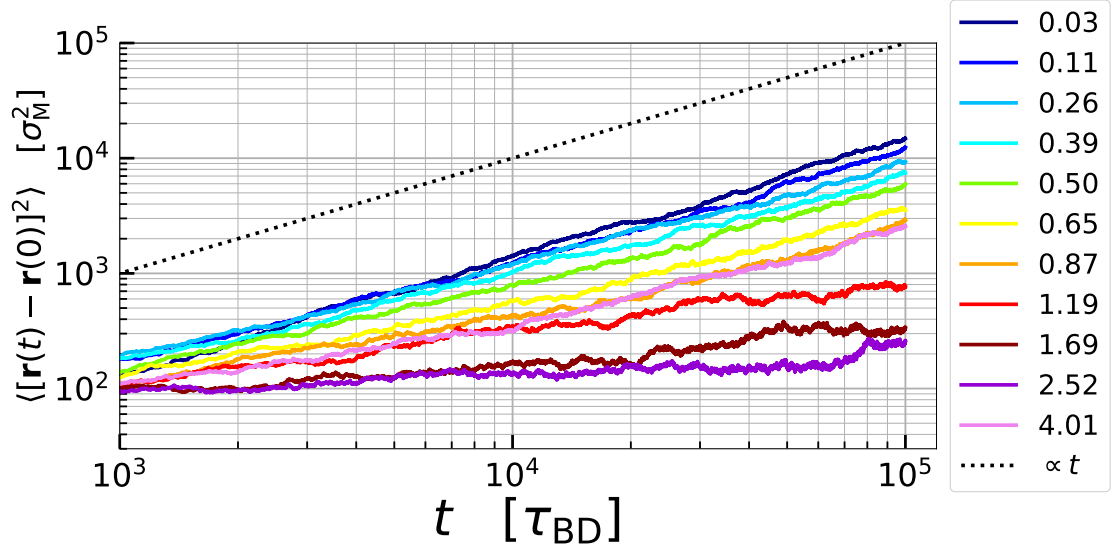


Figure 14: Mean squared displacement of our CG model with property potential $\Psi_4^{poly}(\sigma)$ as a function of time for different packing fractions η (legend on the right). The dashed line represents a linear function $\langle [\mathbf{r}(t) - \mathbf{r}(0)]^2 \rangle = t$.

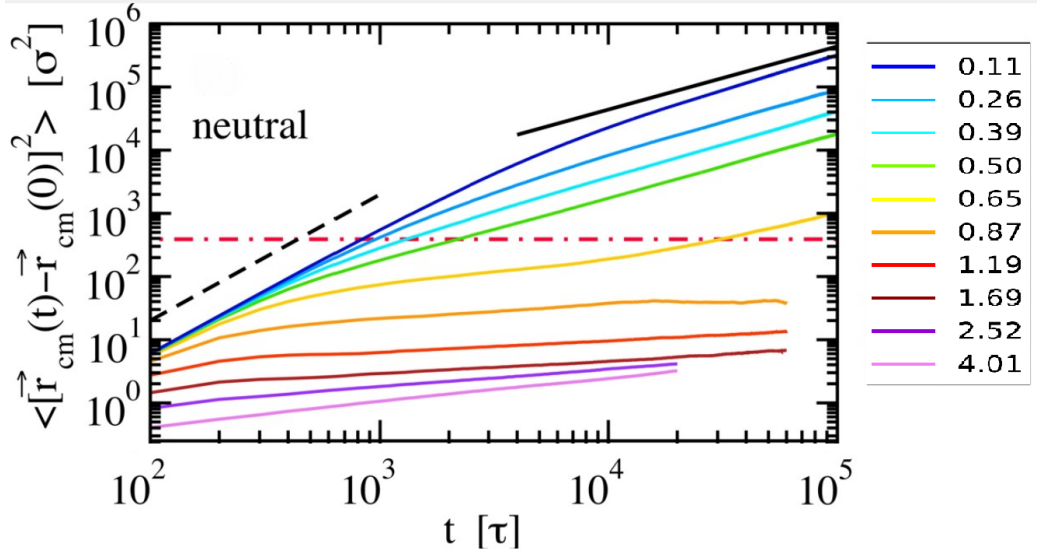


Figure 15: Mean squared displacement of the BN model as a function of time for different packing fractions η (legend on the right). Figure taken from Ref. [16] and legend modified from the original for consistency with current terminology. Published under the terms of the Creative Commons Attribution 4.0 International License (CC BY 4.0).

5.7 Different Property potentials

Until now, we have used a polynomial of order four for the potential of the property $\Psi(\sigma)$ and presented the results in the previous chapter. These results showed a shrinking behavior of the particles and a re-entrant of the main RDF peak height with increasing packing fraction η . However, as shown in fig. 8(a), the particles in the BN model shrink to smaller diameters σ . To achieve similarly low diameters in our CG responsive simulation, we now explore alternative functional forms for the property potential $\Psi(\sigma)$.

5.7 Polynomial Order Two

To achieve lower particle diameters, we use a simple second-order polynomial as an initial guess for the property potential $\Psi(\sigma)$. This functional form is expected to reach lower energy levels at smaller diameters than the previously used polynomial of order four Ψ_4^{poly} . The fitting function for the property potential data $-\frac{1}{\beta} \ln(\tilde{p}_{0.03}^{\text{BN}}(\sigma))$ is defined as

$$\Psi_2^{\text{poly}}(\sigma) = \frac{(\sigma - \sigma_0)^2}{2\delta^2}. \quad (59)$$

Here, the form is chosen so that the corresponding parent function $p(\sigma) = e^{-\beta\Psi_2^{\text{poly}}(\sigma)}$ represents a simple Gaussian distribution. Figure 16 shows the resulting fit to the

data. For this fit, we excluded the data points of the bulge on the right tail in order to better capture the potential well. The resulting fitting parameters are listed in table 3 in the Appendix section 7.2. Comparing the fitted property potential to the previously obtained $\Psi_4^{\text{poly}}(\sigma)$ in fig. 3 shows us a much lower potential curve for smaller diameters σ .

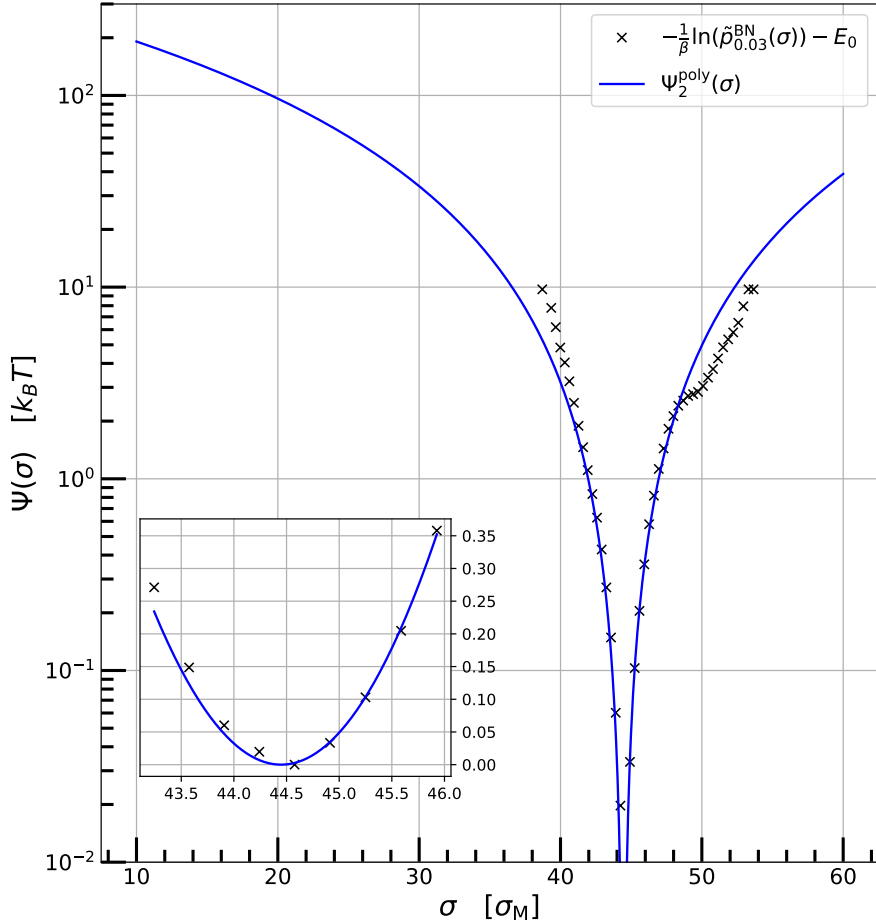


Figure 16: The black crosses show the property potential $\Psi(\sigma) = -k_B T \ln(\tilde{p}_{0.03}^{\text{BN}}(\sigma))$ of the BN system in the LDL. They were calculated from the emergent size distribution $\tilde{p}_{0.03}^{\text{BN}}(\sigma)$ provided by Del Monte and Zaccarelli [16]. $\Psi_2^{\text{poly}}(\sigma)$ (blue line) is the fitted second order polynomial.

With the derived property potential $\Psi_2^{\text{poly}}(\sigma)$, we can now try to find a suitable strength for our Hertzian interaction potential $\phi_c(r, \sigma_i, \sigma_j)$, as shown previously in section 5.2. Through trial and error, we again find that the best parameter is $c = 750 k_B T$. Figure 35 in the Appendix shows the effective potential v_{eff} calculated from $\Psi_2^{\text{poly}}(\sigma)$ and $\phi_{750}(r, \sigma_i, \sigma_j)$ as well as the ones from the other models and from the BN model. With both potentials, we now again perform simulations for different packing fractions between $\eta = 0.03$ and 4.01 .

Emergent size distribution and bulk modulus

We begin by presenting the mean particle diameters $\langle \sigma \rangle$ and their associated variances $\langle \sigma^2 \rangle - \langle \sigma \rangle^2$. For this purpose, we use the emergent size distributions $\tilde{p}_\eta(\sigma)$ obtained from the new simulations together with eq. (50). The resulting mean particle diameter (orange line) along with the mean diameters calculated from the emergent size distributions reported by Del Monte and Zaccarelli[16] (blue line) are shown in fig. 17(a) as a function of the packing fraction η .

At low packing fraction, the particle diameter remains constant in the BN model, while in our CG model it immediately begins to decrease gradually. Then both models show a clear shrinkage of the particles around $\eta = 1$. In addition, the two curves converge to a similar mean particle diameter of $\langle \sigma \rangle \approx 29$ at the highest packing fraction, $\eta = 4.01$. Overall, both models show a comparable trend in the shrinking behavior of the mean diameter with increasing packing fraction.

The dashed line in fig. 17(a) represents the isotropic shrinkage behavior, calculated using eq. (54). It can be seen that our current CG model follows an approximately isotropic shrinking at high packing fractions. This trend is also reflected in the effective packing fraction, shown in fig. 28 in the Appendix section 7.2, where η_{eff} is not yet constant but tends towards a plateau at high densities.

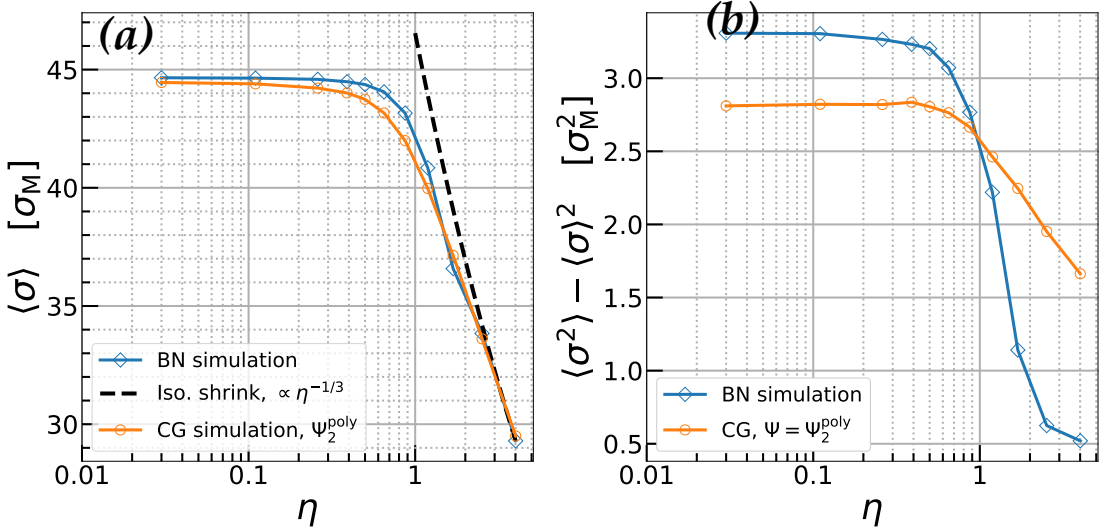


Figure 17: Mean particle sizes (a) and variance (b) calculated with eq. (50) from $\tilde{p}_\eta(\sigma)$ and $\tilde{p}_\eta^{\text{BN}}(\sigma)$. Here $\tilde{p}_\eta(\sigma)$ is determined from the particle sizes of the CG model with the property potential $\Psi_2^{\text{poly}}(\sigma)$ and $\tilde{p}_\eta^{\text{BN}}(\sigma)$ is provided by Del Monte and Zaccarelli [16].

Next, we examine the corresponding variance, $\langle \sigma^2 \rangle - \langle \sigma \rangle^2$, shown in fig. 17(b). The plot reveals a constant behavior at low packing fraction, followed by a significant decrease for $\eta > 1$ for both models. However, our CG model shows a lower initial variance and a more gradual decrease at higher η values. In the end, the BN model reaches a variance of $0.5 \sigma_M^2$, while our model arrives at a value of $\approx 1.6 \sigma_M^2$.

These differences indicate a stiffer response of the CG model at low packing fractions and a softer reaction to increasing particle crowding. This behavior arises from the

use of a second-order polynomial as the property potential, which facilitates particle shrinking compared to the fourth-order potential used before (see fig. 8(b)). The resulting smaller particle diameters at high densities then again provide more space in the system, allowing larger size fluctuations. In contrast, although the particles in the BN model shrink to similar sizes, their internal network structure and the resulting meshing between neighboring particles at high densities restrict equivalent fluctuations.

In the following, we analyze the bulk modulus of the system K and the individual particle bulk modulus K_p . The latter is derived from volume fluctuation (see eq. (15)), which is determined based on the emergent size distributions via eq. (57), introduced in the previous chapter. Figure 18(a) depicts K_p as a function of the packing fraction η . For comparison, we employ the K_p of the BN model, recalculated from spherical volume fluctuation in the same manner as for our system. This recalculation was first introduced for comparison in fig. 10 and is discussed in detail in the accompanying text.

If we now look at the individual bulk modulus of both models, we observe that they follow a similar trend at low packing fractions, gradually increasing with η . However, for $\eta > 1$, the BN model starts to increase more strongly than our CG model. This difference correlates with the variance behavior of both models shown above. Here, the BN model shows a larger decrease at higher packing fractions, resulting in eq. (15) in a higher individual bulk modulus. These observations indicate a softer response of the CG particles under dense packing conditions.

Next, we examine the bulk modulus of the whole system, K . This quantity is obtained from the derivative of the system pressure according to the box volume (eq. (58)). The pressure P as a function of the box volume V is shown in fig. 29 in the appendix. Figure 18(b) compares the calculated bulk modulus with the values reported for the BN model by Del Monte and Zaccarelli [16] as a function of the packing fraction η . The two curves start at low values for K and exhibit an increase with increasing packing fraction. However, similar to the behavior of $\Psi_4^{\text{poly}}(\sigma)$ as a property potential, the BN model reaches significantly larger values than our CG model (see fig. 11(b)). Furthermore, the bulk modulus now only reaches approximately $2.5 \cdot 10^{-3} k_B T / \sigma_M^3$, while previously it reached about $7 \cdot 10^{-3} k_B T / \sigma_M^3$. This result indicates that the CG system responds even more softly to increasing densities, which can be attributed to the enhanced particle shrinkage allowed in the current model.

Radial Distribution Function and Mean Squared Displacement

In the following, we examine the RDF of our current model, presented in fig. 19 together with the $g(r)$ curves of the BN model. For the lowest packing fraction, the RDF reaches approximately 1.2, indicating an already weak particle correlation. For an increasing packing fraction, we observe a growth in height of the main peak and a shift of its position towards smaller distances r . This behavior is consistent with that of

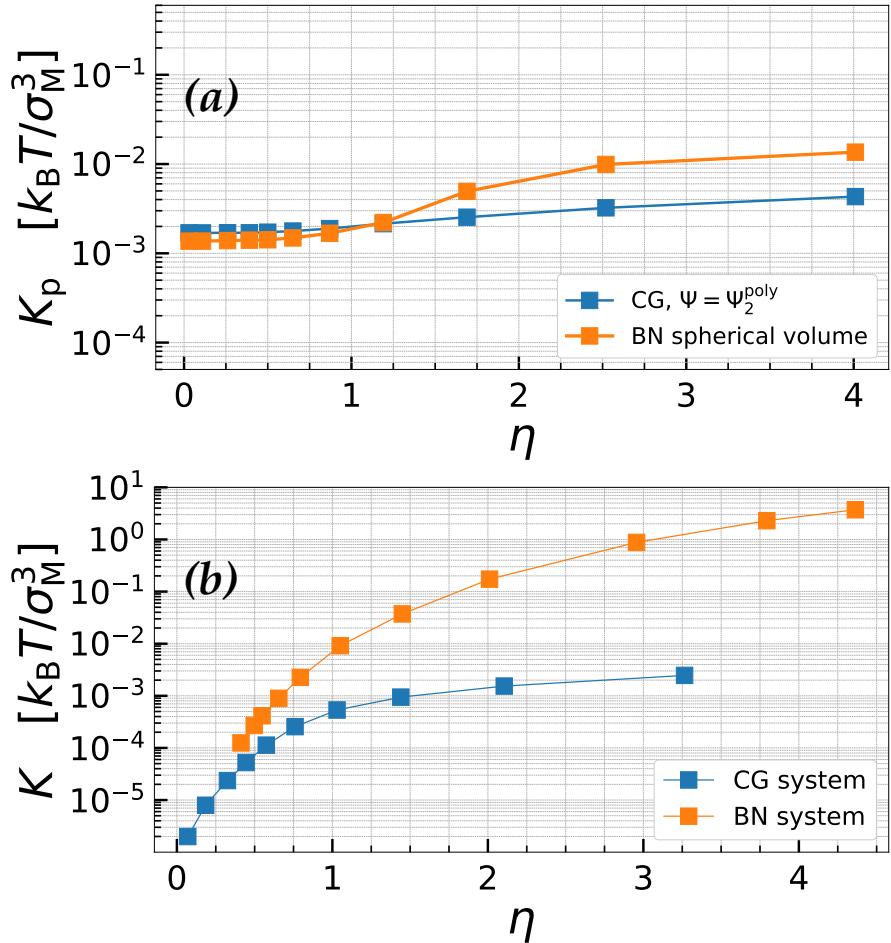


Figure 18: (a): Bulk modulus of individual particles K_p , calculated from spontaneous volume fluctuations (see eq. (15)), dependent on the packing fraction η . The orange line presents K_p of the BN system, where we use the emergent size distribution $\tilde{p}_\eta^{\text{BN}}(\sigma)$ provided by Del Monte and Zaccarelli [16] to calculate the particle volumes (assuming spherical volumes). The blue line reports on K_p of our CG system with a now second order polynomial as the property potential, $\Psi_2^{\text{poly}}(\sigma)$. This is also calculated using the emergent size distribution $\tilde{p}_\eta(\sigma)$ for the volume fluctuations.
 (b): Bulk modulus of the whole system K , calculated directly from the derivative of pressure according to the volume. The orange line shows K from the BN system of Del Monte and Zaccarelli, with the data being directly taken from FIG.8.(b) [16]. The blue line presents K from our CG system with property potential $\Psi_2^{\text{poly}}(\sigma)$ calculated from eq. (58).

the previously used model (see fig. 13) and the BN model at lower packing fractions. The increase in the height of the main peak slows for $\eta > 1$ and gradually reverses between $\eta = 2.52$ and 4.01 . This is a difference from the BN model, where the decrease begins much earlier, around $\eta = 0.8$, and is considerably stronger. The same trend is seen in the previously used CG model, which starts to decrease at $\eta = 1.69$, but much stronger. These observations indicate that the enhanced particle shrinking of the current CG model, compared to the earlier one, allows the system to maintain a more ordered structure at much higher packing densities.

Finally, we examine the MSD of our current model, presented in fig. 30 in the appendix section 7.2. Like the previously used model, it shows diffusive behavior for low packing fractions and a slowdown in dynamics around $\eta = 0.5$. It also depicts the plateau region for mid-time ranges and the following regained particle movement at long times, here starting at $\eta = 2.52$. Overall, we can observe a similar behavior in particle movement as the packing fraction increases.

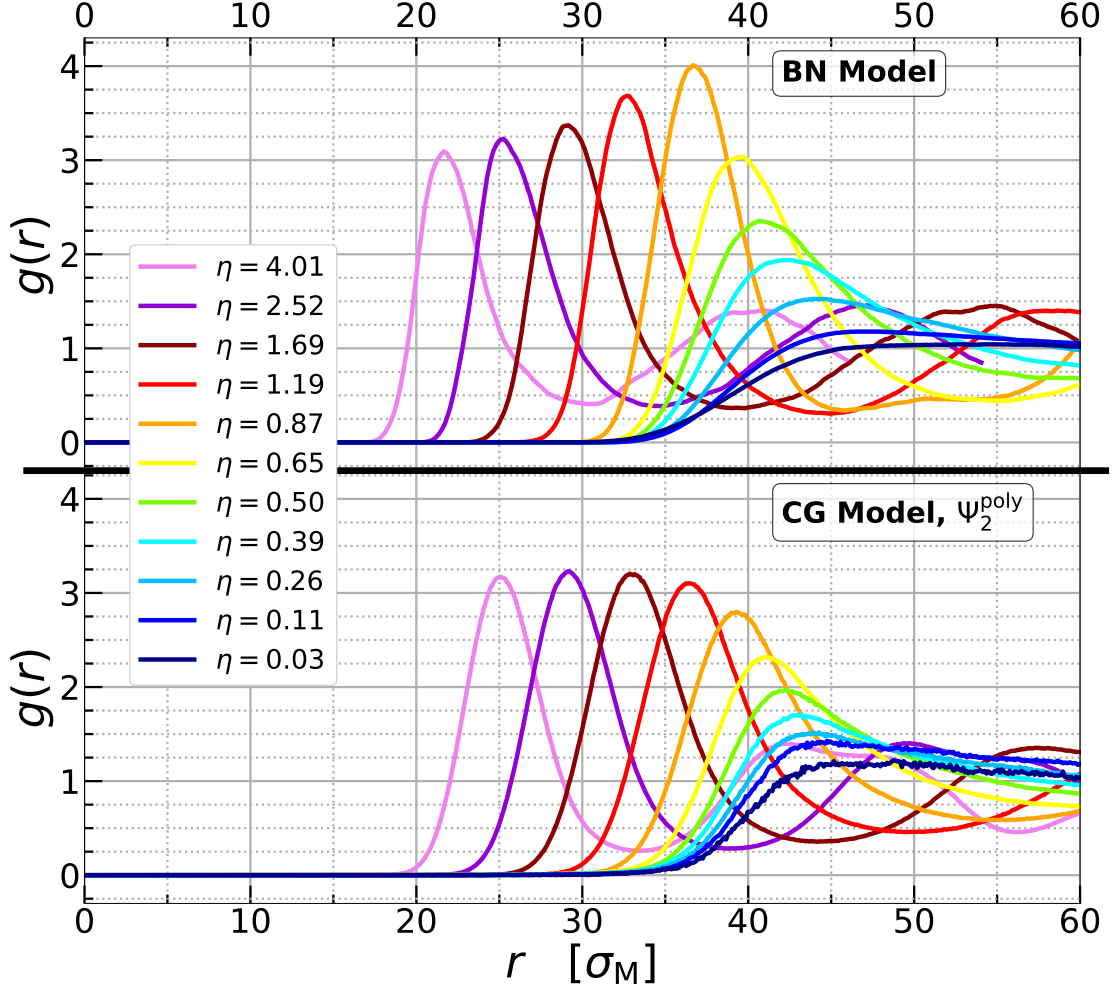


Figure 19: Radial distribution function for different packing fractions η of our CG model with property potential $\Psi_2^{\text{poly}}(\sigma)$ (bottom) and the BN model (top). The $g(r)$ values for the BN model are provided by Del Monte and Zaccarelli [16].

5.7 FENE Potential

The previously used second-order polynomial as the property potential has shown some improvement for our CG model by reaching particle diameters at high packing fractions similar to those of the BN model. However, it failed to reproduce a clear re-entrant behavior of the main $g(r)$ peaks for high densities.

For an alternative approach, we now use a FENE potential, as introduced in eq. (25). Near the equilibrium bond length, the FENE potential behaves similarly to a simple harmonic oscillator but includes a maximum bond length beyond which the potential diverges to infinity. This mathematical form makes the FENE potential an attractive choice for the property potential $\Psi(\sigma)$, with low energies around the equilibrium and a build in upper limit on the particle size.

For fitting the property potential data $-\frac{1}{\beta} \ln(\tilde{p}_{0.03}^{\text{BN}}(\sigma))$ from Del Monte and Zaccarelli, we use a FENE potential of the form

$$\Psi_R^{\text{FENE}}(\sigma) = a \log \left(1 - \left(\frac{\sigma - \sigma_0}{R} \right)^2 \right), \quad (60)$$

with the coefficient a , the equilibrium size σ_0 as fitting parameters and the maximum allowed distance to σ_0 , R as a free parameter. Figure 20 shows the resulting fit to the data with R chosen as $16\sigma_M$. Thereby the maximum distance R is chosen to be close to the desired minimum particle size of the BN model. For the fit, we excluded the data points of the bulge on the right tail in order to better capture the potential well. The fit parameters are shown in table 4. The small plot on the lower left of fig. 20 shows that while the fit function covers the overall trend of the potential well, it is slightly shifted to the left. We also do another fit with $R = 15.5\sigma_M$ presented in fig. 31 in the appendix section 7.3.

For the two derived FENE potentials, $\Psi_{R=16}^{\text{FENE}}$ and $\Psi_{R=15.5}^{\text{FENE}}$, we select the parameter for the Hertzian potential $\phi_c(r, \sigma_i, \sigma_j)$ as $c = 750 k_B T$, consistent with the previous determination. Figure 35 in the Appendix shows the effective potential v_{eff} calculated from $\Psi_R^{\text{FENE}}(\sigma)$ and $\phi_{750}(r, \sigma_i, \sigma_j)$, respectively, as well as those from the other models and from the BN model.

Using both models, we again perform simulations for different packing fractions in the range $\eta = 0.03$ and 4.01 .

Emergent size distribution and bulk modulus

We begin by presenting the mean particle diameters $\langle \sigma \rangle$, and their associated variances, $\langle \sigma^2 \rangle - \langle \sigma \rangle^2$, for both FENE-based CG models and the BN model, as done previously. The resulting mean particle diameters, together with the mean diameters calculated from the emergent size distributions reported by Del Monte and Zaccarelli[16], are shown in fig. 21(a) as a function of the packing fraction η .

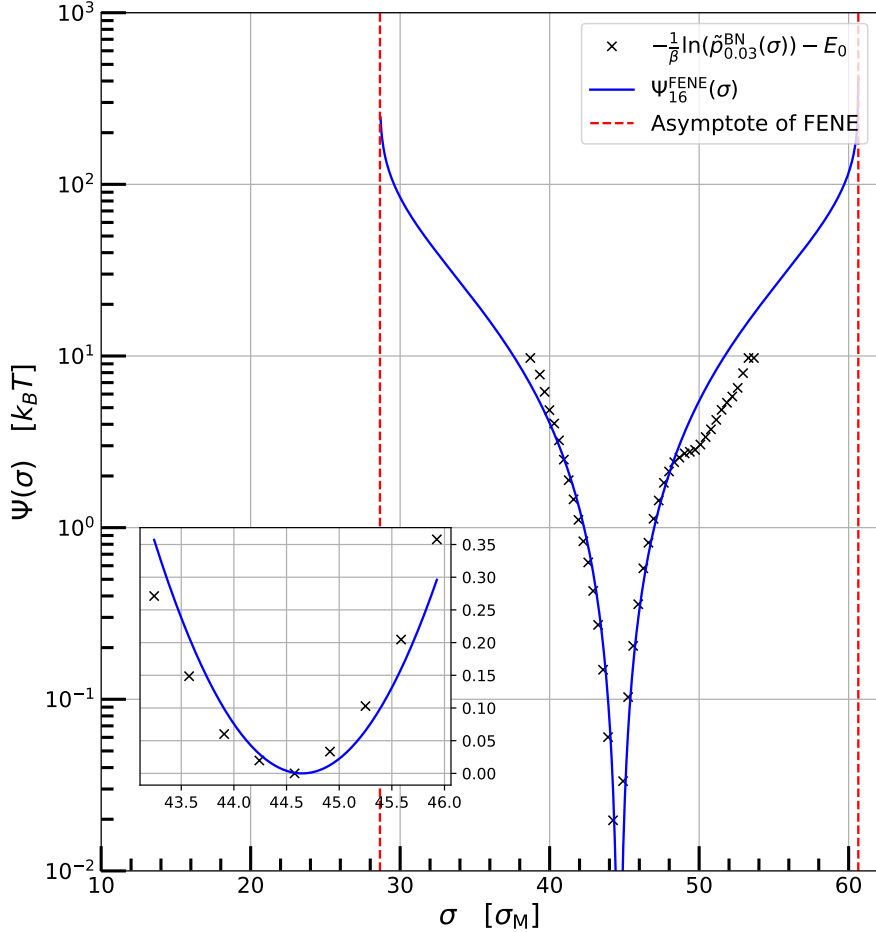


Figure 20: The black crosses show the property potential $\Psi(\sigma) = -k_B T \ln(\tilde{p}_{0.03}^{\text{BN}}(\sigma))$ of the BN system in the LDL. They were calculated from the emergent size distribution $\tilde{p}_{0.03}^{\text{BN}}(\sigma)$ provided by Del Monet and Zaccarelli [16]. $\Psi_{R=16}^{\text{FENE}}(\sigma)$ (blue line) is the fitted FENE potential with the maximum distance to the equilibrium size $R = 16 \sigma_M$.

At low packing fraction, the particle diameter remains constant in the BN model, while in our CG models it begins to gradually decrease around $\eta = 0.1$. In the CG model with $R = 15.5 \sigma_M$, particle shrinkage starts already around $\eta = 0.50$ and continues to a value of $\approx 30 \sigma_M$ at the highest density. Although this final diameter is similar to that reached by the BN model, our model exhibits a much steeper decrease with increasing η and only minor size changes between the last two packing fractions. This suggests that the particle sizes reached are already close to the vertical asymptote of $\Psi_{R=15.5}^{\text{FENE}}$, resulting in a reduced shrinkage. A possible explanation for the steeper decrease could be that the FENE potential is not sufficiently strong.

The FENE model with $R = 16 \sigma_M$ also exhibits stronger particle shrinkage than the BN model at a packing fraction of about one. However, this trend reverses for $\eta > 1$, where our CG FENE model shrinks more slowly and already ends at a particle size of approximately $33 \sigma_M$. This behavior indicates a soft response of our CG model compared to the BN model for packing fractions $\eta < 1$, and a comparatively harder

response at higher packing fractions.

The dashed line in fig. 21(a) represents the reference line for isotropic shrinkage, calculated from eq. (54) using the highest packing fraction of the BN model data. The $\Psi_{R=16}^{\text{FENE}}$ model deviates clearly from the reference curve, exhibiting a much less steep decrease. This behavior arises from the increased stiffness of the particles, which hinders further shrinkage. The $\Psi_{R=15.5}^{\text{FENE}}$ model follows a trend more similar to the BN data, but still differs from the reference line. Especially at the highest packing fraction, where the mean particle diameters approach the vertical asymptote of the FENE potential, effectively preventing additional shrinkage.

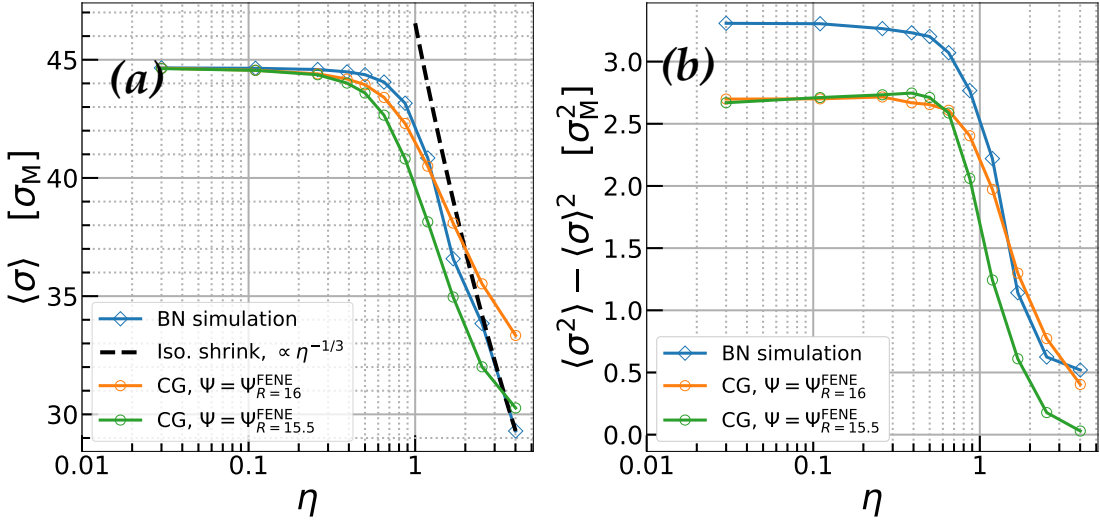


Figure 21: Mean particle sizes (a) and variance (b) calculated with eq. (50) from $\tilde{p}_\eta^R(\sigma)$ and $\tilde{p}_\eta^{BN}(\sigma)$. Here $\tilde{p}_\eta^{BN}(\sigma)$ is provided by Del Monte and Zaccarelli [16], while $\tilde{p}_\eta^R(\sigma)$ comes from the CG models with $\Psi_{R=15.5}^{\text{FENE}}$ and $\Psi_{R=16}^{\text{FENE}}$, respectively.

Next, we examine the corresponding variance, $\langle \sigma^2 \rangle - \langle \sigma \rangle^2$, shown in fig. 21(b). The plot reveals a constant behavior at low packing fraction, followed by a significant decrease for $\eta > 1$ for both FENE-based CG models. Although a similar trend is shown by the BN model, it starts at a higher initial variance. That behavior was also observed in the CG model based on the second-order polynomial for the property potential in fig. 17(b). While the CG model with $R = 16$ follows the decrease in variance of the BN model for $\eta < 1$, the other CG model with $R = 15.5$ σ_M exhibits a stronger decrease reaching almost zero. This indicates again that in this model the particle sizes are getting too close to the vertical asymptote of the FENE potential, resulting in almost no particle size changes. This can also be seen in the emergent size distributions shown in fig. 32 in the Appendix section 7.3.

The effective packing fractions of both CG models are presented in fig. 33 in the appendix section 7.3. $\Psi_{R=16}^{\text{FENE}}$ shows a trend similar to the first CG model used, based on a fourth-order polynomial for $\psi(\sigma)$, shown in fig. 9. $\Psi_{R=15.5}^{\text{FENE}}$ on the other hand, exhibits a more curved trend for $\eta < 2$, similar to the second CG model with Ψ_2^{poly} in fig. 28. However, for larger packing fractions, it again exhibits a much steeper increase.

In the following, we analyze the bulk modulus of individual particles K_p , calculated as in the previous cases and presented in fig. 22. The CG model based on $\Psi_{R=16}^{\text{FENE}}$ exhibits a constant bulk modulus at low packing fractions ($\eta < 1$) and from there increases with η , following a similar trend as the BN model. In contrast, the model based on $\Psi_{R=15.5}^{\text{FENE}}$ shows a much larger increase in K_p for $\eta > 1$, reaching values an order of magnitude higher than those of the other two models at the highest density. This indicates a much stiffer response of the particle to compression than in the other cases. Overall, these results highlight the sensitivity of the particle mechanics to the choice of the FENE-based property potential parameter R .

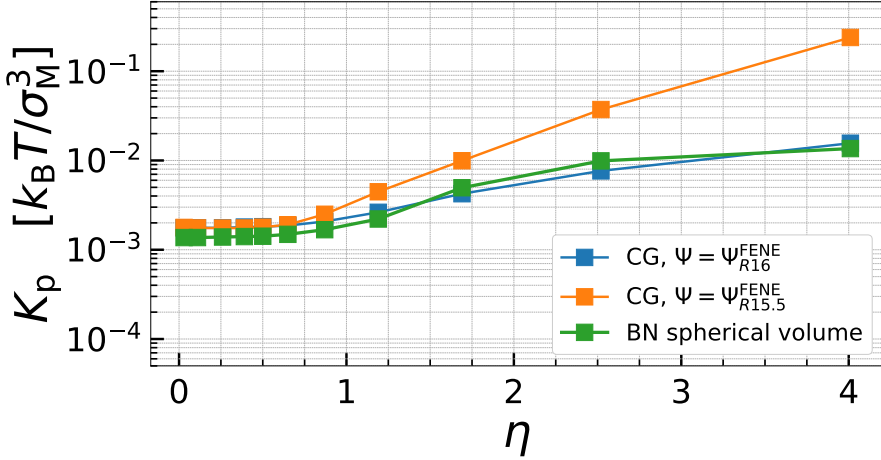


Figure 22: Bulk modulus of individual particles K_p , calculated from spontaneous volume fluctuations (see eq. (15)), dependent on the packing fraction η . The green line presents K_p of the BN system, where we use the emergent size distribution $\tilde{p}_\eta^{\text{BN}}(\sigma)$ provided by Del Monte and Zaccarelli [16] to calculate the particle volumes (assuming spherical volumes). The blue line represents the current CG model with $\Psi_{R=16}^{\text{FENE}}$ and the orange line the current CG model with $\Psi_{R=15.5}^{\text{FENE}}$. These are also calculated using the emergent size distribution $\tilde{p}_\eta^R(\sigma)$ for the volume fluctuations, respectively.

Next, we examine the bulk modulus of the whole system, K , as previously obtained from the derivative of the system pressure according to the box volume. The pressure P as a function of the box volume V for both CG FENE-based models is shown in fig. 34 in the Appendix. Figure 23 compares the calculated bulk modulus with the values reported for the BN model by Del Monte and Zaccarelli[16] as a function of the packing fraction η . Panel (a) shows the model with $\Psi_{R=15.5}^{\text{FENE}}$ as the property potential, and panel (b) the model with $\Psi_{R=16}^{\text{FENE}}$. Both bulk moduli start at low values and exhibit an increase with rising packing fraction. However, the $\Psi_{R=15.5}^{\text{FENE}}$ model exhibits a steeper increase, resulting in a bulk modulus approximately an order of magnitude higher K than that of the other CG model at the highest density. This indicates significant stiffer particle behavior, consistent with the trend observed in the individual particle bulk modulus and the size variance for this model. Nevertheless, both models yield substantially lower K values than the BN model.

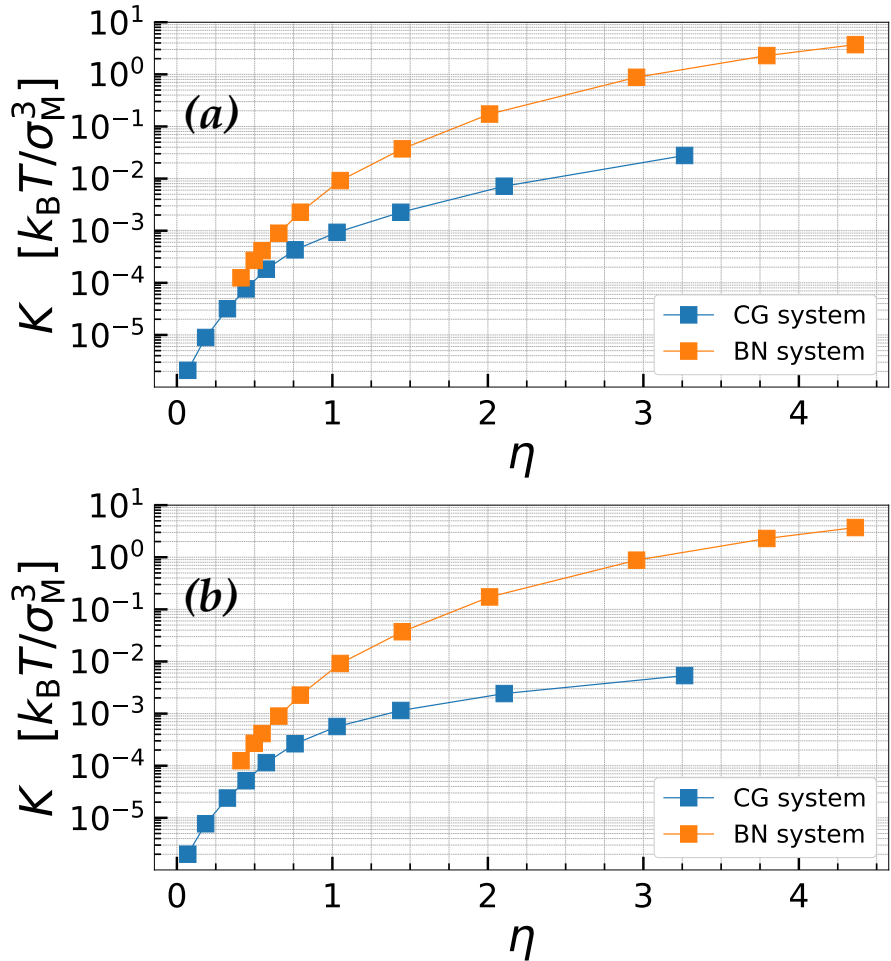


Figure 23: Bulk modulus of the whole system K , calculated directly from the derivation of pressure according to the volume. The orange line shows K from the BN system of Del Monte and Zaccarelli, with the data being directly taken from FIG.8.(b) [16]. (a) shows the CG model with $\Psi_{R=15.5}^{\text{FENE}}$ and (b) the one with $\Psi_{R=16}^{\text{FENE}}$.

Radial Distribution Function and Mean Squared Displacement

In the following, we take a look at the $g(r)$ curves of the two FENE-based CG models. Figure 24 shows the model with $\Psi_{R=15.5}^{\text{FENE}}$ as the property potential, while fig. 25 shows the model with $\Psi_{R=16}^{\text{FENE}}$ with the $g(r)$ curves of the BN model above them, respectively.

As observed in the CG model with the second-order polynomial as $\Psi(\sigma)$, both FENE-based models display a main peak slightly above one at the lowest packing fraction. With increasing packing fraction η , the peak height increases and shifts its position to smaller distances. The $\Psi_{R=15.5}^{\text{FENE}}$ model exhibits a significant stronger increase in peak height, reaching a maximum of approximately 6.25 at $\eta = 2.52$. In contrast, the $\Psi_{R=16}^{\text{FENE}}$ model reaches a maximum of around 3.5 at $\eta = 1.69$. On contrast, the BN model reaches a maximum height of 4 at $\eta = 0.8$. This makes all used CG responsive models

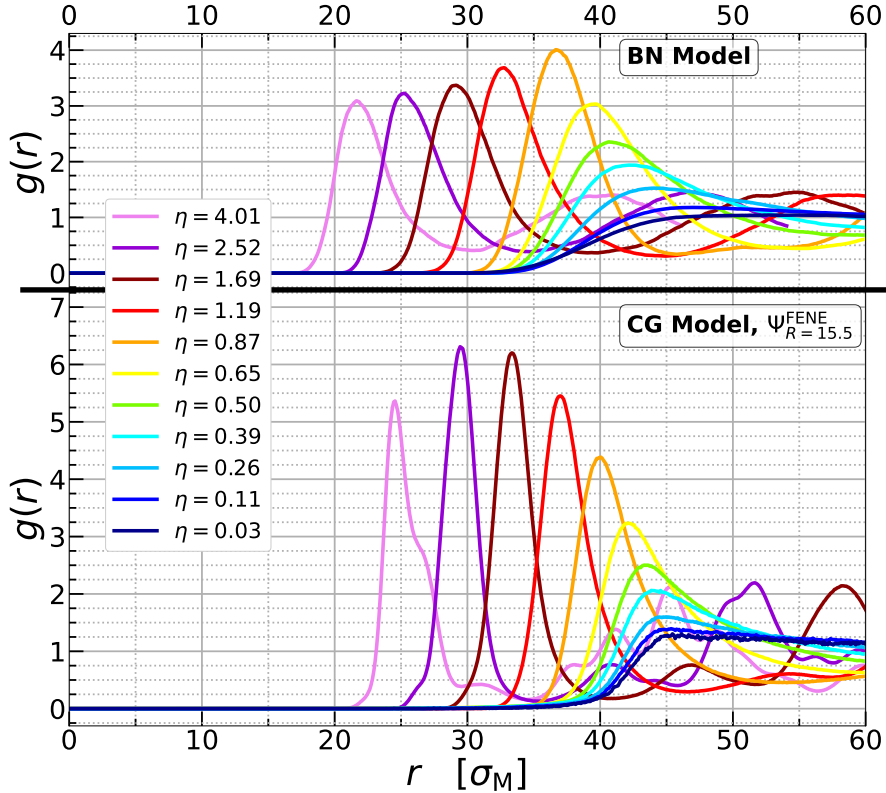


Figure 24: Radial distribution function for different packing fractions η of our CG model with property potential $\Psi_{R=15.5}^{\text{FENE}}$ (bottom) and the BN model (top). The $g(r)$ values for the BN model are provided by Del Monte and Zaccarelli [16].

reach their maximum later than the BN model.

Similarly to the CG model based on a fourth-order polynomial and the BN model, both FENE-based models show a decrease in the main peak high after reaching their respective maximum. Overall, the $\Psi_{R=15.5}^{\text{FENE}}$ model shows a much more structured system than the other CG models, even after the re-entering of the $g(r)$ curve.

Finally, we examine the MSD of the two FENE-based models, presented in fig. 26. Similar to the previously analyzed CG models, both models show diffusive behavior for low packing fractions and a slowdown in dynamics starting around $\eta = 0.5$. A plateau region is observed at intermediate times, followed by a recovery of particle motion at long times. The regime of near-zero dynamics at high packing fractions is more pronounced in both models. In particular, the $\Psi_{R=15.5}^{\text{FENE}}$ model shows almost no movement at the three highest packing fractions, suggesting that the system may not yet have fully equilibrated.

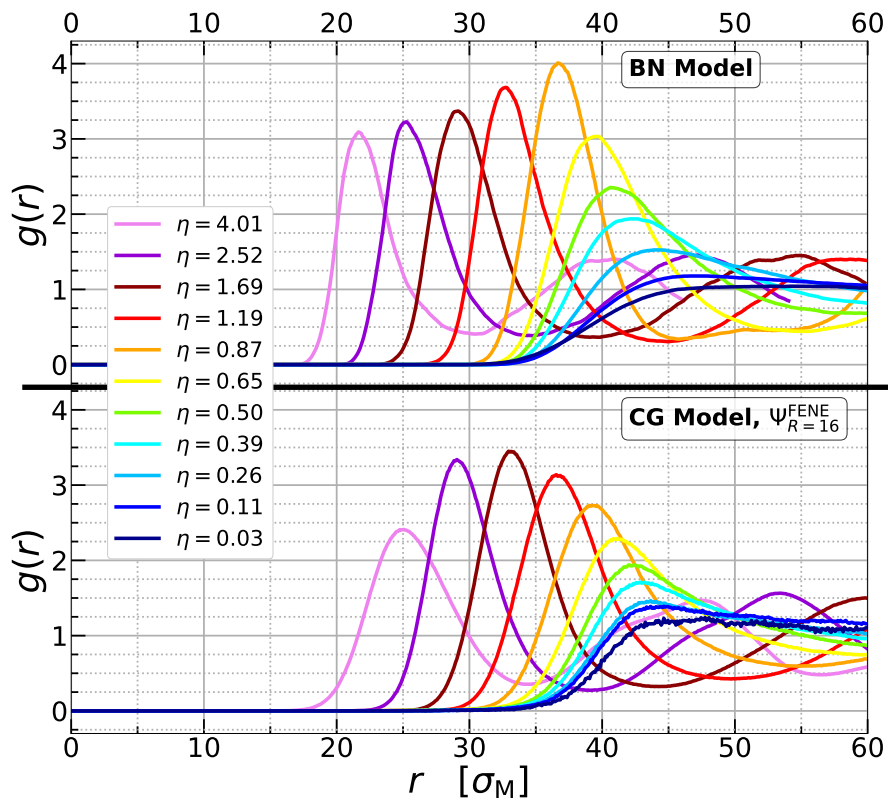


Figure 25: Radial distribution function for different packing fractions η of our CG model with property potential $\Psi_{R=16}^{\text{FENE}}$ (bottom) and the BN model (top). The $g(r)$ values for the BN model are provided by Del Monte and Zaccarelli [16].

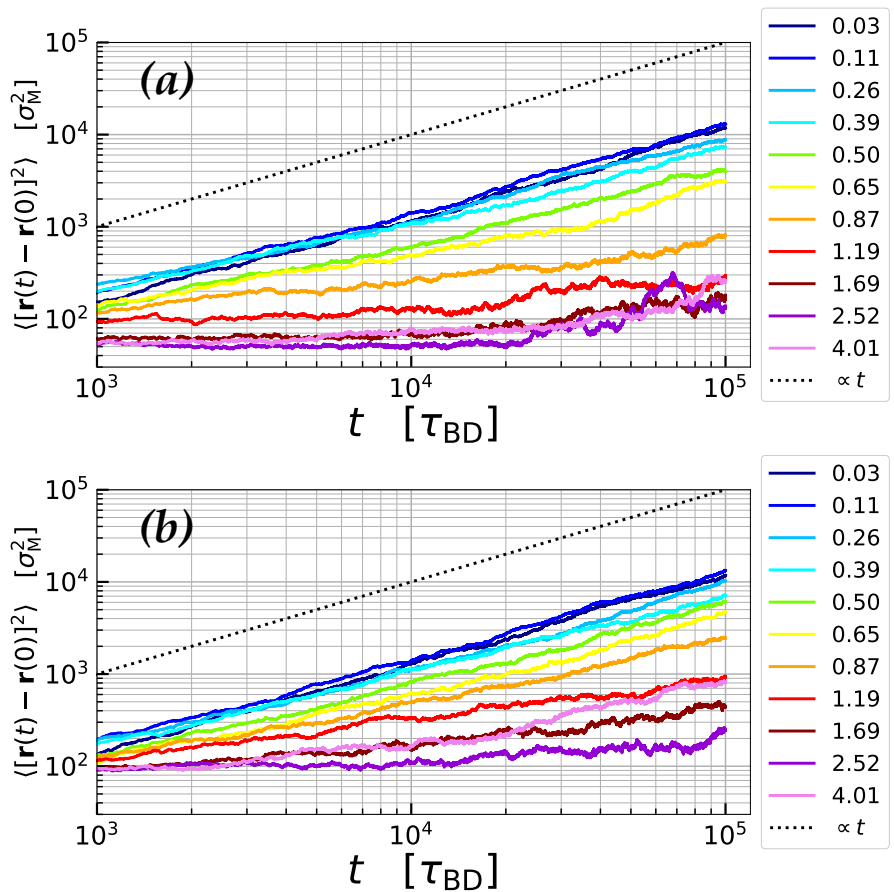


Figure 26: Mean squared displacement for different packing fractions η . Panel (a) shows the CG model with $\Psi_{R=15.5}^{FENE}$ and panel (b) the one with $\Psi_{R=16}^{FENE}$. The dashed line represents a linear function $\langle [\mathbf{r}(t) - \mathbf{r}(0)]^2 \rangle = t$.

6 Conclusion and Outlook

The aim of this thesis was to identify a suitable property and interaction potential for a coarse-grained (CG) simulation model of responsive colloids (RC) capable of reproducing the behavior of the bead-network (BN) simulations performed by Del Monte and Zaccarelli [16]. To this end, we extracted an effective property potential $\Psi(\sigma)$ from the emergent size distribution of the BN system in the low-density limit and fitted it to different polynomials and FENE-like functions, namely: $\Psi_2^{\text{poly}}(\sigma)$, $\Psi_4^{\text{poly}}(\sigma)$, $\Psi_{R=15.5}^{\text{FENE}}(\sigma)$ and $\Psi_{R=16}^{\text{FENE}}(\sigma)$. For the particle interaction, we employed a Hertzian two-body interaction with a potential strength parameter that depends on the particle diameter. The resulting CG models were studied on a wide range of packing fractions and compared to the BN reference in terms of structural, mechanical, and dynamical properties.

In general, the CG models successfully captured the qualitative behavior of the BN system. All functions tested for $\Psi(\sigma)$ reproduced the essential responsive feature of particle shrinkage with increasing packing fraction.

The individual particle and system bulk moduli showed a significant discrepancy between the tested models and the BN model. This discrepancy arises from the different levels of coarse-graining and the soft nature of the Hertzian potential in our models. However, the recalculated individual particle bulk moduli, now assuming a spherical volume change, of the BN model show a trend and order of magnitude similar to those of our CG tested models.

The models also showed the expected structural behavior: the emergence of short-range order at intermediate densities and a re-entrant decrease of order at higher densities. However, this re-entrant behavior occurs in all tested CG models at much higher packing fractions than in the BN model. This is due to the isotropic shrinkage of individual particles, which creates more free volume at high packing fractions. As a consequence, its structural ordering remains up to larger packing fractions, and the maximum of the $g(r)$ peak occurs later than in the BN model.

Their dynamics followed the same general pattern as the BN system: initially diffusive and slowing down upon compression. However, they partially recovered mobility at high packing fractions.

Among the property potentials tested, none were capable of perfectly reproducing all simulation data of the BN model performed by Del Monte and Zaccarelli. Although the model with the polynomial property potential $\Psi_2^{\text{poly}}(\sigma)$ provided the closest agreement in terms of mean particle diameter, it did not exhibit a clear re-entrant structural behavior. In contrast, the model with the FENE-based property potential with $R = 16\sigma_M$, while less accurate in reproducing the mean particle diameters of the BN model, captured the characteristic re-entrant trend in the radial distribution function. Furthermore, it provided the most coherent overall behavior across structural,

mechanical, and dynamical observables. For this reason, it is the most suitable CG model among our tested potentials.

Outlook

Despite the remaining quantitative differences, the results highlight that we can find suitable one- and two-body potentials for the CG responsive-particle framework, so it is capable of reproducing the essential physics of the BN system of Del Monte and Zaccarelli.

With targeted refinements—such as flexible forms of the property potential $\Psi(\sigma)$ —a closer quantitative match to the BN simulations should be achievable without sacrificing the computational efficiency of the coarse-grained approach. For example, a piecewise construction of $\Psi(\sigma)$ for the different diameter σ regimes could enhance the property potential. Specifically, a high-order polynomial could be used to fit the LDL data of the BN simulations, along a less steep, FENE-like function for the regime of smaller diameters where we do not have direct fitting data. At present, the FENE-based property potential exhibits the most promising results for the small diameter regime. It is not too steep, allowing particles to reach sufficiently small diameters, while also demonstrating re-entrant behavior in $g(r)$ through a much stronger increase near R .

Until now, we have always used the same form for the interaction potential $\phi(r, \sigma_i, \sigma_j)$, assuming that the simple Hertzian potential with diameter-dependent strength parameter is sufficient to describe particle-particle interactions, while focusing on the property potential. This approach was a much simpler for the overall model but represents a point where we can improve the CG framework. For example, one could divide the interaction potential into different regimes, such as an inner core and an outer shell regime, as presented by Moncho-Jordá *et al.* [18].

7 Appendix

7.1 Transformation from Radius of Gyration to Real Diameter

For the transformation, we use the formula for the radius of gyration eq. (22). Because we do not know the exact locations of each monomer, we use a density profile $\rho(r)$ to describe the microgels from Del Monte and Zaccarelli. The simulated soft microgels can be described by the fuzzy sphere model[16] and this gives us a density profile $\rho_{\text{Sphere}}^{\text{Fuzzy}}(r)$ following eq. (12). With the continuous function $\rho_{\text{Sphere}}^{\text{Fuzzy}}(r)$ the radius of gyration calculates to

$$R_g^2 = \frac{\int r^2 \rho_{\text{Sphere}}^{\text{Fuzzy}}(r) dr}{\int \rho_{\text{Sphere}}^{\text{Fuzzy}}(r) dr} = \frac{\int_0^\infty r^4 \rho_{\text{Sphere}}^{\text{Fuzzy}}(r) dr}{\int_0^\infty r^2 \rho_{\text{Sphere}}^{\text{Fuzzy}}(r) dr} \quad (61)$$

$$\begin{aligned} &= \frac{\rho_0 \int_0^{R_C} r^4 dr + \rho_0 \int_{R_C}^\infty r^4 \operatorname{erfc}\left(\frac{r-R_C}{\sqrt{2}\sigma_{\text{surf}}}\right) dr}{\rho_0 \int_0^{R_C} r^2 dr + \rho_0 \int_{R_C}^\infty r^2 \operatorname{erfc}\left(\frac{r-R_C}{\sqrt{2}\sigma_{\text{surf}}}\right) dr} \\ &= \frac{\frac{R_C^5}{5} \left[1 + 5\sqrt{\frac{2}{\pi}} \left(\frac{\sigma_{\text{surf}}}{R_C} \right) + 10 \left(\frac{\sigma_{\text{surf}}}{R_C} \right)^2 + 20\sqrt{\frac{2}{\pi}} \left(\frac{\sigma_{\text{surf}}}{R_C} \right)^3 + 15 \left(\frac{\sigma_{\text{surf}}}{R_C} \right)^4 + 8\sqrt{\frac{2}{\pi}} \left(\frac{\sigma_{\text{surf}}}{R_C} \right)^5 \right]}{\frac{R_C^3}{3} \left[1 + 3\sqrt{\frac{2}{\pi}} \left(\frac{\sigma_{\text{surf}}}{R_C} \right) + 3 \left(\frac{\sigma_{\text{surf}}}{R_C} \right)^2 + 2\sqrt{\frac{2}{\pi}} \left(\frac{\sigma_{\text{surf}}}{R_C} \right)^3 \right]} \end{aligned} \quad (62)$$

$$(63)$$

We then use the Taylor expansion around zero $\frac{a}{1+x} \approx a[1 - x + O(x^2)]$ and estimate $\sigma_{\text{surf}} \ll R_C$:

$$R_g^2 \approx \frac{3}{5} R_C^2 \left[1 + 5\sqrt{\frac{2}{\pi}} \left(\frac{\sigma_{\text{surf}}}{R_C} \right) + 10 \left(\frac{\sigma_{\text{surf}}}{R_C} \right)^2 + 20\sqrt{\frac{2}{\pi}} \left(\frac{\sigma_{\text{surf}}}{R_C} \right)^3 \right. \quad (64)$$

$$\left. + 15 \left(\frac{\sigma_{\text{surf}}}{R_C} \right)^4 + 8\sqrt{\frac{2}{\pi}} \left(\frac{\sigma_{\text{surf}}}{R_C} \right)^5 \right] \quad (65)$$

$$\cdot \left[1 - 3\sqrt{\frac{2}{\pi}} \left(\frac{\sigma_{\text{surf}}}{R_C} \right) - 3 \left(\frac{\sigma_{\text{surf}}}{R_C} \right)^2 - 2\sqrt{\frac{2}{\pi}} \left(\frac{\sigma_{\text{surf}}}{R_C} \right)^3 \right] \quad (66)$$

$$\approx \frac{3}{5} R_C^2 \left[1 + 2\sqrt{\frac{2}{\pi}} \left(\frac{\sigma_{\text{surf}}}{R_C} \right) + \left(7 - \frac{30}{\pi} \right) \left(\frac{\sigma_{\text{surf}}}{R_C} \right)^2 + O\left(\left(\frac{\sigma_{\text{surf}}}{R_C}\right)^3\right) \right] \quad (67)$$

This gives us at the end

$$R_g^2 \approx \frac{3}{5} R_C^2 + \frac{6}{5} \sqrt{\frac{2}{\pi}} (R_C \sigma_{\text{surf}}) + \frac{3}{5} \left(7 - \frac{30}{\pi} \right) \sigma_{\text{surf}}^2. \quad (68)$$

The first term corresponds to R_g of a hard sphere with radius R_C while the other two terms represent first and second order corrections because of the fuzzy shell. With eq. (68) until first order correction and the relation $R = R_C + 2\sigma_{\text{surf}}$ the real radius is given by

$$R = \frac{5}{3} \sqrt{\frac{\pi}{2}} \frac{R_g^2}{R_C} - \left(\sqrt{\frac{\pi}{2}} - 1 \right) R_C \quad (69)$$

7.2 Plots and Tables for second order polynomial

Table 3: Fit Parameters for fitting $-k_B T \ln(\tilde{p}_{0.03}^{BN}(\sigma))$ with $\Psi_2^{\text{poly}}(\sigma)$ eq. (59).

$\delta [\sigma_M / k_B T]$	$s_0 [\sigma_M]$
1.76 ± 0.03	44.45 ± 0.06

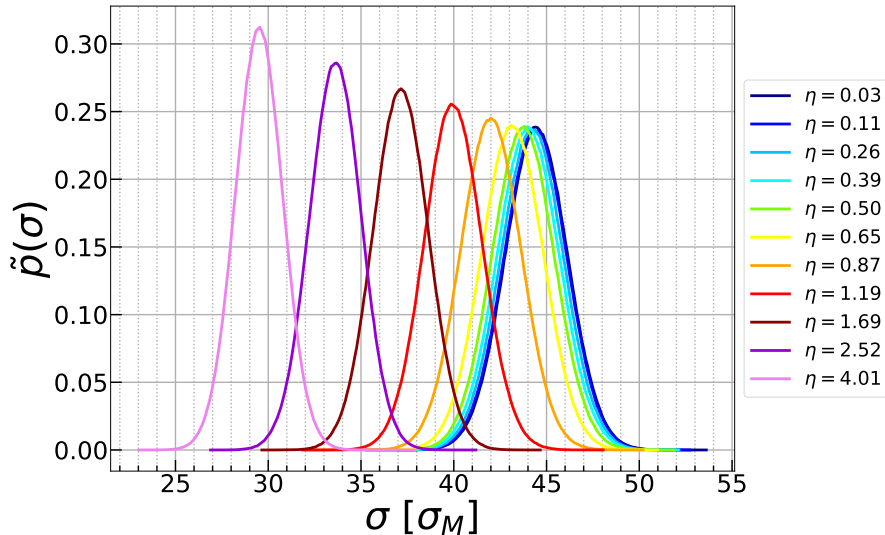


Figure 27: Emergent size distributions $\tilde{p}_\eta(\sigma)$ for increasing packing fractions η from right to left for the CG model based on the second order polynomial as the property potential.

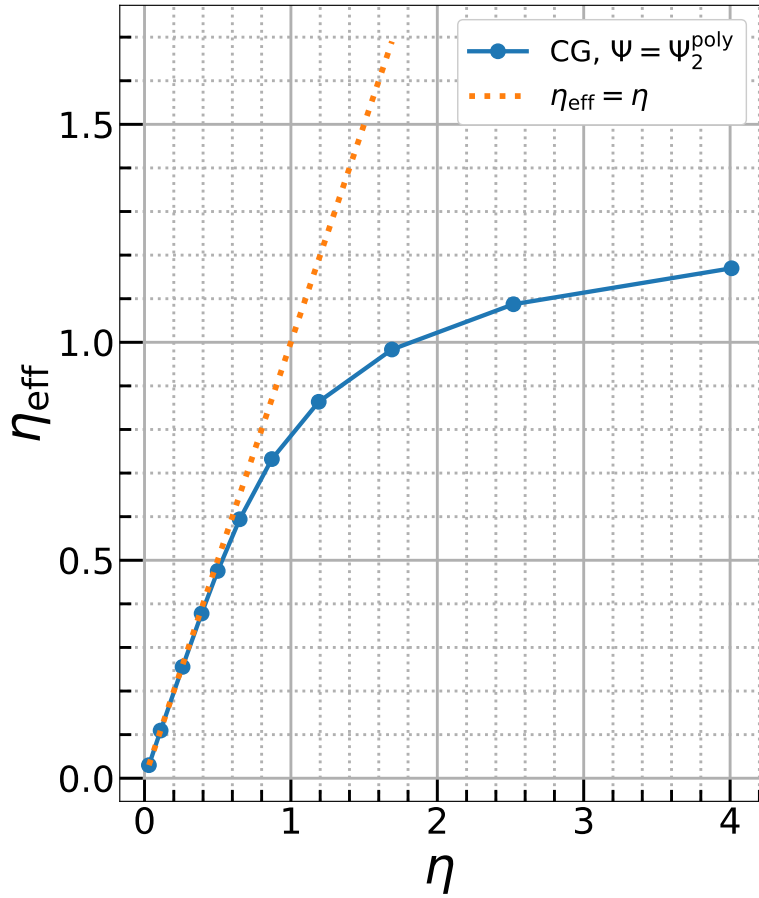


Figure 28: Effective packing fraction η_{eff} as a function of the packing fraction η , for the CG model based on the second order polynomial as the property potential. η_{eff} is thereby calculated from the mean particle size $\langle \sigma \rangle_\eta$. The dotted line shows $\eta_{\text{eff}} = \eta$, representing the case of a non responsive system.

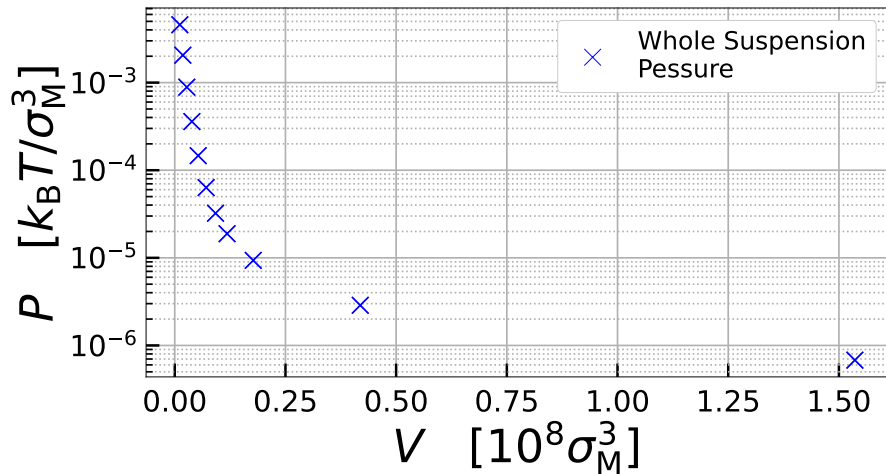


Figure 29: System pressure P calculated using the virial equation of state (eq. (13)), for the CG model based on the second order polynomial as the property potential.

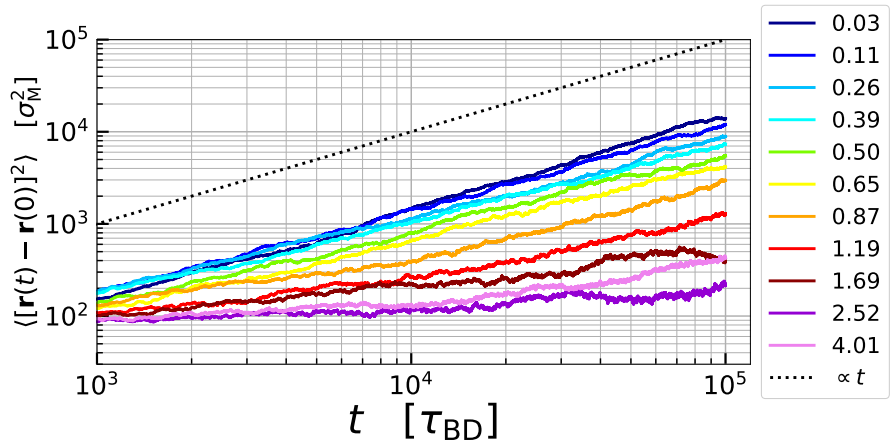


Figure 30: Mean squared displacement as a function of time for different packing fractions η (legend on the right), for the CG model based on the second order polynomial as the property potential. The dashed line represents a linear function $\langle [\mathbf{r}(t) - \mathbf{r}(0)]^2 \rangle = t$.

7.3 Plots and Tables for the FENE potentials

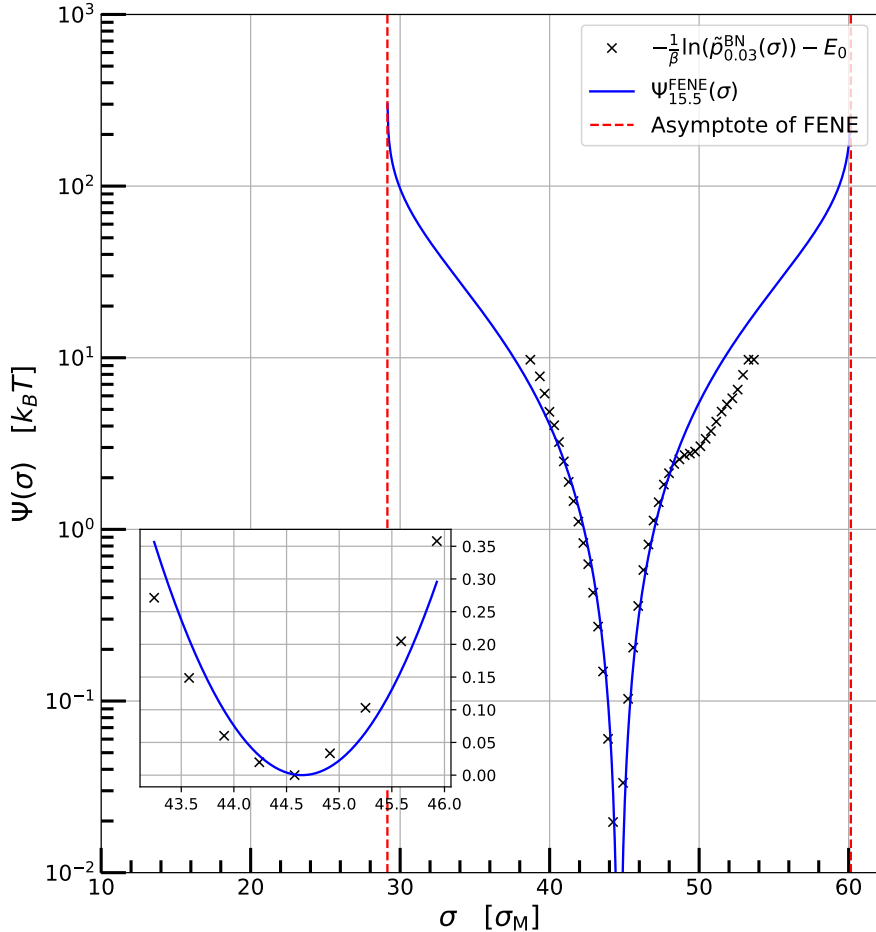


Figure 31: The black crosses show the property potential $\Psi(\sigma) = -k_B T \ln(\tilde{p}_{0.03}^{BN}(\sigma))$ of the BN system in the LDL. They were calculated from the emergent size distribution $\tilde{p}_{0.03}^{BN}(\sigma)$ provided by Del Monet and Zaccarelli[16]. $\Psi_{R=15.5}^{\text{FENE}}(\sigma)$ (blue line) is the fitted FENE potential with the maximum distance to the equilibrium size $R = 15.5 \sigma_M$.

Table 4: Fit Parameters for fitting $-k_B T \ln(\tilde{p}_{0.03}^{BN}(\sigma))$ with $\Psi_R^{\text{FENE}}(\sigma)$ eq. (60) for different maximum distances to the equilibrium size R .

$R [\sigma_M]$	$a [k_B T]$	$s_0 [\sigma_M]$	$R [\sigma_M]$	$a [k_B T]$	$s_0 [\sigma_M]$
16	-46.1 ± 1.1	44.64 ± 0.04	15.5	-43.2 ± 1.0	44.65 ± 0.04

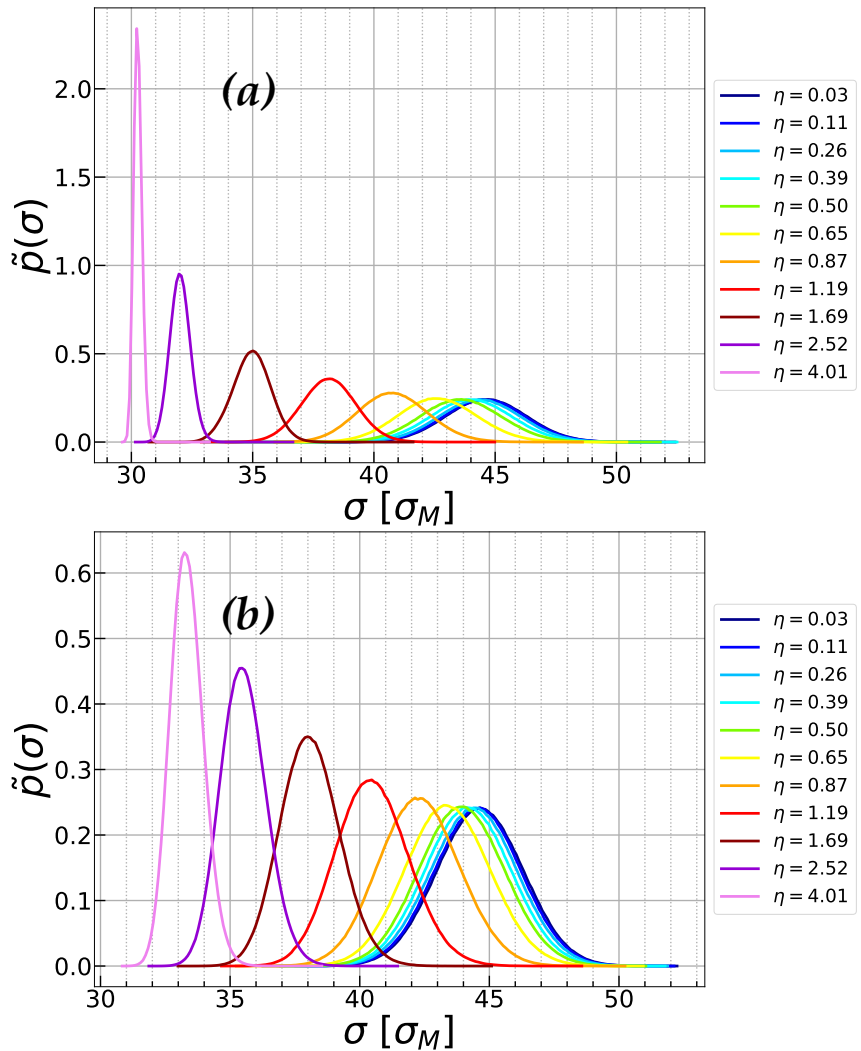


Figure 32: Emergent size distributions $\tilde{p}_\eta(\sigma)$ for increasing packing fractions η from right to left. **(a)** shows the CG model based on the FENE with $R = 15.5 \sigma_M$ and **(b)** shows the CG model based on the FENE with $R = 16 \sigma_M$.

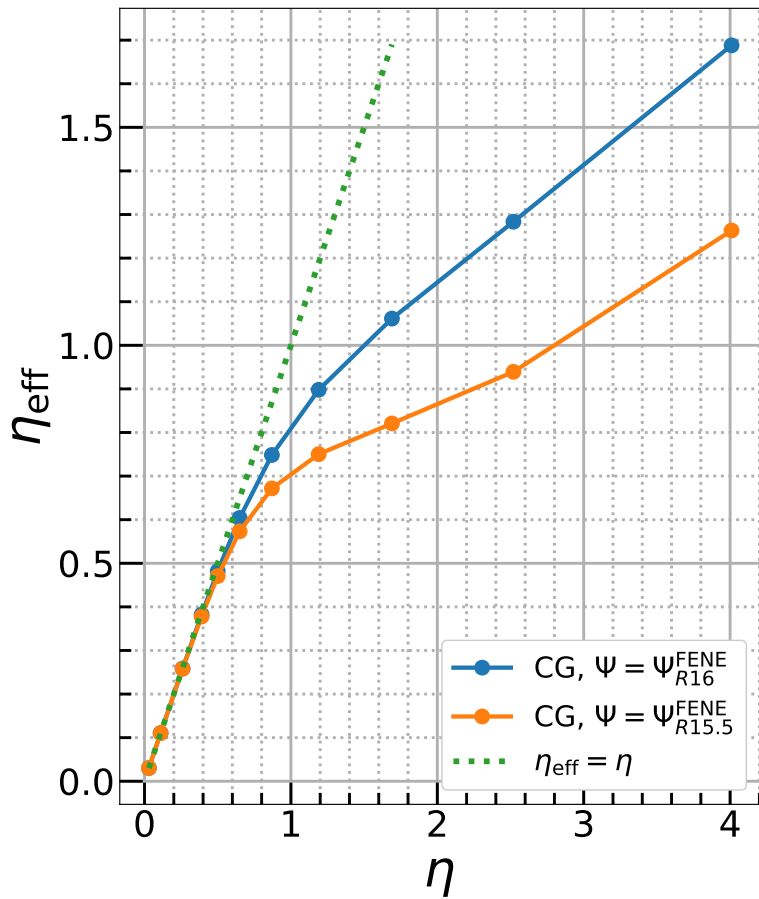


Figure 33: Effective packing fraction η_{eff} as a function of the packing fraction η , for the CG model based on the FENE potentials with $R = 15.5 \sigma_M$ and $R = 16 \sigma_M$. η_{eff} is thereby calculated from the mean particle size $\langle \sigma \rangle_\eta$. The dotted line shows $\eta_{\text{eff}} = \eta$, representing the case of a non responsive system.

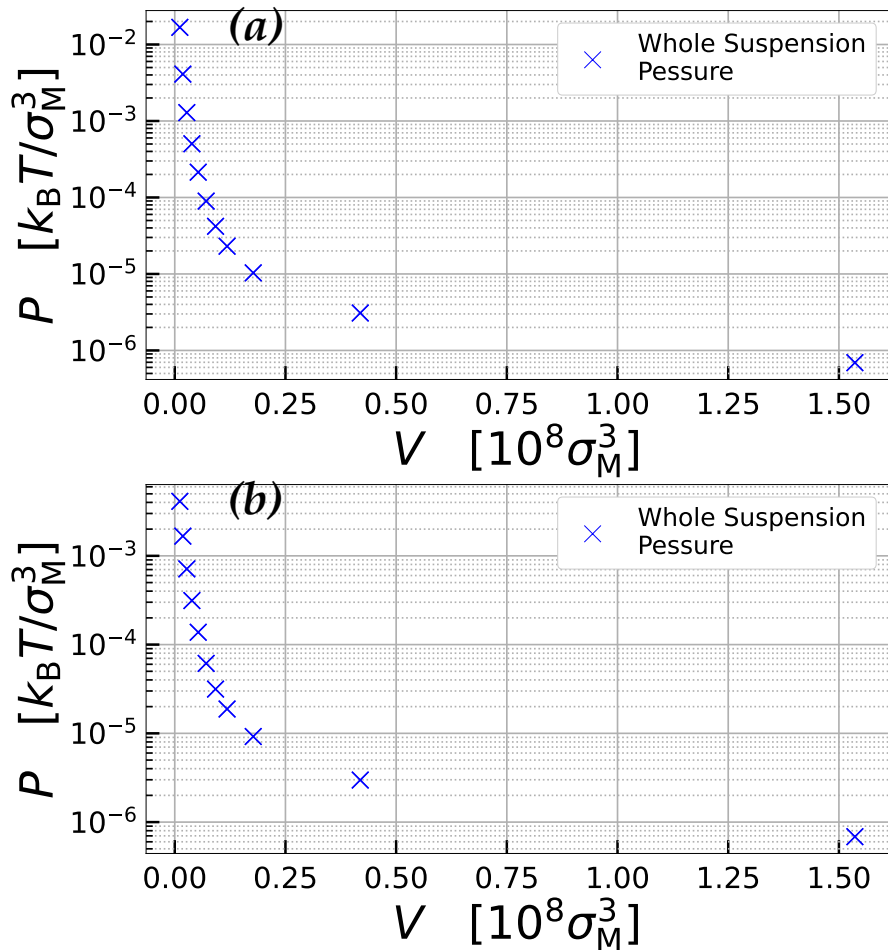


Figure 34: System pressure P calculated using the virial equation of state (eq. (13)), for the CG model based on the FENE potential with (a) $R = 15.5 \sigma_M$ and (b) $R = 16 \sigma_M$.

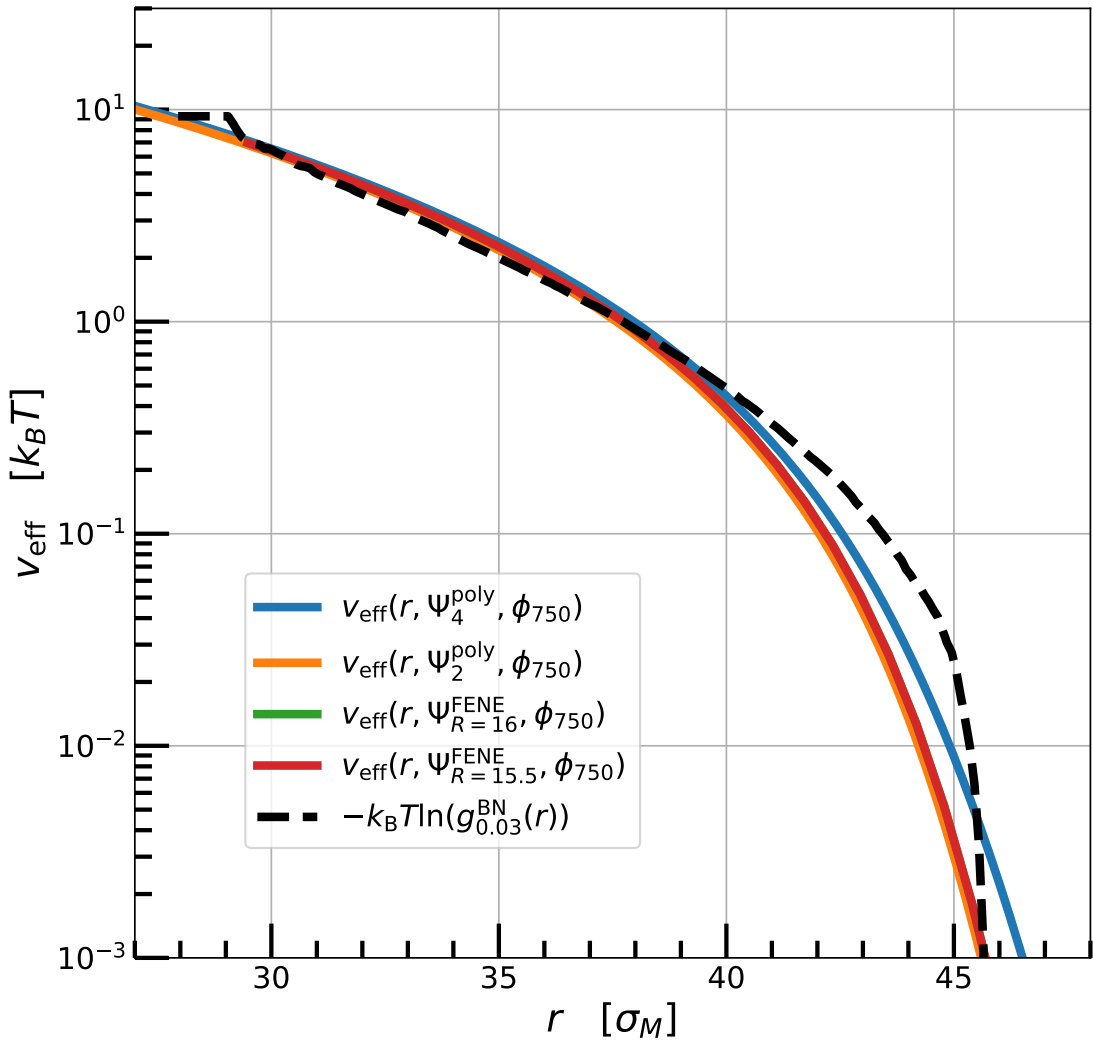


Figure 35: The dashed line shows the effective potential in the LDL of the BN simulation calculated from the radial distribution function $g_{0.03}^{BN}(r)$ from Del Monte and Zaccarelli [16]. The colored lines represent effective potentials calculated from eq. (31), using the different tested property potentials Ψ and the interaction potential $\phi_{750}(r, \sigma_i, \sigma_j)$.

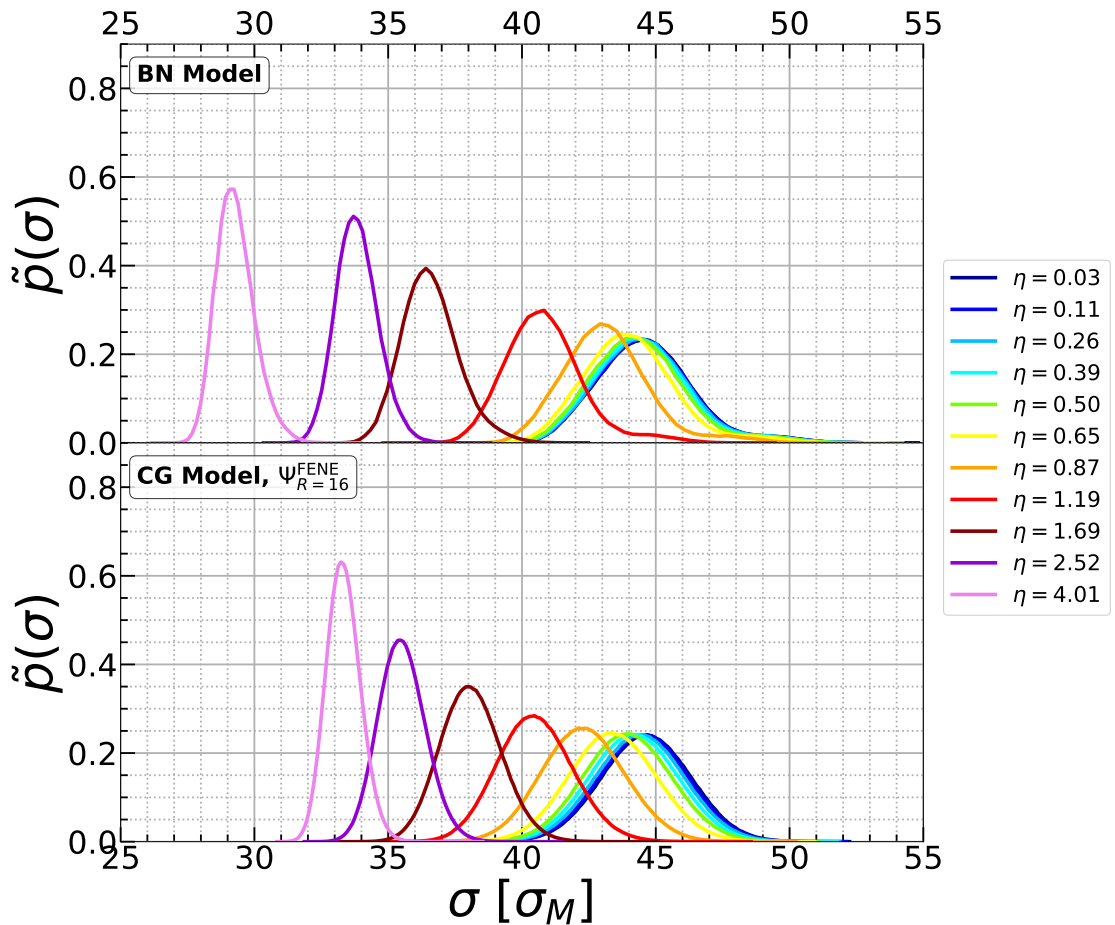


Figure 36: Emergent size distribution $\tilde{p}_\eta^{\text{BN}}(\sigma)$ from the BN model, provided by Del Monet and Zaccarelli[16] and $\tilde{p}_\eta(\sigma)$ from the CG model with $\Psi_{R=16}^{\text{FENE}}$ for different packing fractions η .

References

- ¹J. Brijitta and P. Schurtenberger, "Responsive hydrogel colloids: structure, interactions, phase behavior, and equilibrium and nonequilibrium transitions of microgel dispersions", *Current Opinion in Colloid & Interface Science* **40**, 87–103 (2019) 10.1016/j.cocis.2019.02.005.
- ²B. R. Saunders, N. Laajam, E. Daly, S. Teow, X. Hu, and R. Stepto, "Microgels: from responsive polymer colloids to biomaterials", *Advances in Colloid and Interface Science* **147–148**, 251–262 (2009) 10.1016/j.cis.2008.08.008.
- ³P. J. Yunker, K. Chen, M. D. Gratale, M. A. Lohr, T. Still, and A. G. Yodh, "Physics in ordered and disordered colloidal matter composed of poly(n-isopropylacrylamide) microgel particles", *Reports on Progress in Physics* **77**, 056601 (2014) 10.1088/0034-4885/77/5/056601.
- ⁴F. A. Plamper and W. Richtering, "Functional microgels and microgel systems", *Accounts of Chemical Research* **50**, 131–140 (2017) 10.1021/acs.accounts.6b00544.
- ⁵A. Balcerak-Woźniak, M. Dzwonkowska-Zarzycka, and J. Kabatc-Borcz, "A comprehensive review of stimuli-responsive smart polymer materials—recent advances and future perspectives", *Materials* **17**, 4255 (2024) 10.3390/ma17174255.
- ⁶A. Scotti, A. R. Denton, M. Brugnoni, J. E. Houston, R. Schweins, I. I. Potemkin, and W. Richtering, "Deswelling of microgels in crowded suspensions depends on cross-link density and architecture", *Macromolecules* **52**, 3995–4007 (2019) 10.1021/acs.macromol.9b00729.
- ⁷D. Paloli, P. S. Mohanty, J. J. Crassous, E. Zaccarelli, and P. Schurtenberger, "Fluid–solid transitions in soft-repulsive colloids", *Soft Matter* **9**, 3000 (2013) 10.1039/c2sm27654b.
- ⁸I. Bouhid de Aguiar, T. van de Laar, M. Meireles, A. Bouchoux, J. Sprakel, and K. Schroën, "Deswelling and deformation of microgels in concentrated packings", *Scientific Reports* **7** (2017) 10.1038/s41598-017-10788-y.
- ⁹P. Otto, S. Bergmann, A. Sandmeyer, M. Dirksen, O. Wrede, T. Hellweg, and T. Huser, "Resolving the internal morphology of core–shell microgels with super-resolution fluorescence microscopy", *Nanoscale Advances* **2**, 323–331 (2020) 10.1039/c9na00670b.
- ¹⁰P. Voudouris, D. Florea, P. van der Schoot, and H. M. Wyss, "Micromechanics of temperature sensitive microgels: dip in the poisson ratio near the lcst", *Soft Matter* **9**, 7158 (2013) 10.1039/c3sm50917f.
- ¹¹H. Mohapatra, T. M. Kruger, T. I. Lansakara, A. V. Tivanski, and L. L. Stevens, "Core and surface microgel mechanics are differentially sensitive to alternative crosslinking concentrations", *Soft Matter* **13**, 5684–5695 (2017) 10.1039/c7sm00727b.
- ¹²G. M. Conley, P. Aebsicher, S. Nöjd, P. Schurtenberger, and F. Scheffold, "Jamming and overpacking fuzzy microgels: deformation, interpenetration, and compression", *Science Advances* **3** (2017) 10.1126/sciadv.1700969.

- ¹³Y.-C. Lin, B. Rotenberg, and J. Dzubiella, “Structure and position-dependent properties of inhomogeneous suspensions of responsive colloids”, *Physical Review E* **102**, 042602 (2020) 10.1103/physreve.102.042602.
- ¹⁴P. G. Bolhuis, A. A. Louis, and J. P. Hansen, “Many-body interactions and correlations in coarse-grained descriptions of polymer solutions”, *Physical Review E* **64**, 021801 (2001) 10.1103/physreve.64.021801.
- ¹⁵U. Baul and J. Dzubiella, “Structure and Dynamics of Responsive Colloids with Dynamical Polydispersity”, *Journal of Physics: Condensed Matter* **33**, 174002 (2021) 10.1088/1361-648x/abdbaa.
- ¹⁶G. Del Monte and E. Zaccarelli, “Numerical Study of Neutral and Charged Microgel Suspensions: From Single-Particle to Collective Behavior”, *Physical Review X* **14**, 041067 (2024) 10.1103/physrevx.14.041067.
- ¹⁷S. V. Nikolov, A. Fernandez-Nieves, and A. Alexeev, “Behavior and mechanics of dense microgel suspensions”, *Proceedings of the National Academy of Sciences* **117**, 27096–27103 (2020) 10.1073/pnas.2008076117.
- ¹⁸A. Moncho-Jordá, A. Cuetos, M. A. Fernandez-Rodriguez, J. Dzubiella, and A. Patti, “Capturing structure and morphology in responsive microgels: from intrinsic free energy to collective behavior”, *Macromolecules* **58**, 10659–10676 (2025) 10.1021/acs.macromol.5c01988.
- ¹⁹S. Nedelcu and J.-U. Sommer, “Charged polymers transport under applied electric fields in periodic channels”, *Materials* **6**, 3007–3021 (2013) 10.3390/ma6073007.
- ²⁰S. Hocine and M.-H. Li, “Thermoresponsive self-assembled polymer colloids in water”, *Soft Matter* **9**, 5839 (2013) 10.1039/c3sm50428j.
- ²¹W. Zhang and H. Choi, “Stimuli-responsive polymers and colloids under electric and magnetic fields”, *Polymers* **6**, 2803–2818 (2014) 10.3390/polym6112803.
- ²²M. Kanamala, W. R. Wilson, M. Yang, B. D. Palmer, and Z. Wu, “Mechanisms and biomaterials in ph-responsive tumour targeted drug delivery: a review”, *Biomaterials* **85**, 152–167 (2016) 10.1016/j.biomaterials.2016.01.061.
- ²³O. J. Cayre, J. Hitchcock, M. S. Manga, S. Fincham, A. Simoes, R. A. Williams, and S. Biggs, “Ph-responsive colloidosomes and their use for controlling release”, *Soft Matter* **8**, 4717 (2012) 10.1039/c2sm00002d.
- ²⁴S. C. Sutradhar, N. Banik, G. A. K. M. R. Bari, and J.-H. Jeong, “Polymer network-based nanogels and microgels: design, classification, synthesis, and applications in drug delivery”, *Gels* **11**, 761 (2025) 10.3390/gels11090761.
- ²⁵Z. Li, Q. Fan, and Y. Yin, “Colloidal self-assembly approaches to smart nanostructured materials”, *Chemical Reviews* **122**, 4976–5067 (2021) 10.1021/acs.chemrev.1c00482.
- ²⁶S. Kumari, M. Avais, and S. Chattopadhyay, “Microgels as smart polymer colloids for sensing and environmental remediation”, *ACS Applied Polymer Materials* **5**, 1626–1645 (2023) 10.1021/acsapm.2c01947.

- ²⁷A. Ninarello, J. J. Crassous, D. Paloli, F. Camerin, N. Gnan, L. Rovigatti, P. Schurtenberger, and E. Zaccarelli, "Modeling Microgels with a Controlled Structure across the Volume Phase Transition", *Macromolecules* **52**, 7584–7592 (2019) 10.1021/acs.macromol.9b01122.
- ²⁸L. Rovigatti, N. Gnan, A. Ninarello, and E. Zaccarelli, "Connecting Elasticity and Effective Interactions of Neutral Microgels: The Validity of the Hertzian Model", *Macromolecules* **52**, 4895–4906 (2019) 10.1021/acs.macromol.9b00099.
- ²⁹J. Dzubiella, *Computational physics:material science*, Lecture script, Institute of Physics - University of Freiburg, Version 0.4, 2025.
- ³⁰Z. Schuss, *Brownian dynamics at boundaries and interfaces: in physics, chemistry, and biology* (Springer New York, 2013), 10.1007/978-1-4614-7687-0.
- ³¹F. Scheffold, "Revisiting the density profile of the fuzzy sphere model for microgel colloids", *Soft Matter* **20**, 8181–8184 (2024) 10.1039/d4sm01045k.
- ³²M. Schneider, R. Michels, V. Pipich, G. Goerigk, V. Sauer, H.-P. Heim, and K. Huber, "Morphology of blends with cross-linked pmma microgels and linear pmma chains", *Macromolecules* **46**, 9091–9103 (2013) 10.1021/ma401889k.
- ³³S. Marín-Aguilar and E. Zaccarelli, *Predicting structure and swelling of microgels with different crosslinker concentrations combining machine-learning with numerical simulations*, 2025, 10.48550/ARXIV.2502.07482.
- ³⁴J.-P. Hansen, *Theory of simple liquids, With applications to soft matter*, edited by I. R. McDonald, Fourth edition, Description based on publisher supplied metadata and other sources. (Elsevier, Amsterdam, 2013), 1619 pp.
- ³⁵P. A. Tipler, *Physik*, edited by D. Gerlich, Neuaufl, Spektrum Lehrbuch, Erg. bildet: James S. Walker: Arbeitsbuch zu Tiplers Physik (Spektrum Akad. Verl., Heidelberg [u.a.], 2004), 1522 pp.
- ³⁶M. Rubinstein and R. H. Colby, *Polymer physics*, repr. (Oxford Univ. Press, Oxford [u.a.], 2014), 440 pp.

Erklärung gem. der geltenden Prüfungsordnung:

Hiermit versichere ich, dass

1. ich die eingereichte Masterarbeit bzw. bei einer Gruppenarbeit meinen Anteil entsprechend gekennzeichneten Anteil der Arbeit selbständig verfasst habe,
2. ich keine anderen als die angegebenen Quellen und Hilfsmittel benutzt und alle wörtlich oder sinngemäß aus anderen Werken übernommenen Inhalte als solche kenntlich gemacht habe und
3. die eingereichte Masterarbeit weder vollständig noch in wesentlichen Teilen Gegenstand eines anderen Prüfungsverfahrens war oder ist.

Nirchzarten, 17.11.25

Ort, Datum

S.P. Hauser
Unterschrift

Auszug Prüfungsordnung M.Sc.

Vom 19. August 2005 (Amtliche Bekanntmachungen Jg. 36, Nr. 46, S. 269–293) in der Fassung vom 25. September 2020 (Amtliche Bekanntmachungen Jg. 51, Nr. 66, S. 328–337)

§20 (8) Bei der Einreichung hat der/die Studierende schriftlich zu versichern, dass

1. er/sie die eingereichte Masterarbeit beziehungsweise bei einer Gruppenarbeit seinen/ihren entsprechend gekennzeichneten Anteil der Arbeit selbständig verfasst hat,
2. er/sie keine anderen als die angegebenen Quellen und Hilfsmittel benutzt und alle wörtlich oder sinngemäß aus anderen Werken übernommenen Inhalte als solche kenntlich gemacht hat und
3. die eingereichte Masterarbeit weder vollständig noch in wesentlichen Teilen Gegenstand eines anderen Prüfungsverfahrens war oder ist.